Composite Functional Materials
2025, 1(2): 20250203 https://doi.org/10.63823/20250203

RESEARCH ARTICLE

Photocatalytic H_2O_2 production over $Ti(HPO_4)_2$ S-scheme heterojunction through push-pull electronic effects enhance the oxygen reduction

Shanyue He[a], Xin Zhang[a], Mei Chen[a], Hongquan Jiang[a,*], Yang Qu[b,*], Yanduo Liu[a,*], Jizhou Jiang[c,*]

a. School of Chemistry and Chemical Engineering, Harbin Normal University, Harbin 150025, P. R. China
b. Key Laboratory of Functional Inorganic Materials Chemistry (Ministry of Education), School of Chemistry and Materials Science, International Joint Research Center for Catalytic Technology, Heilongjiang University, Harbin 150080, P. R. China
c. School of Materials Science and Engineering, State Key Laboratory of Green and Efficient Development of Phosphorus Resources, Engineering Research Center of Phosphorus Resources Development and Utilization of Ministry of Education, Key Laboratory of Green Chemical Engineering Process of Ministry of Education, Hubei Key Laboratory of Plasma Chemistry and Advanced Materials, Novel Catalytic Materials of Hubei Engineering Research Center, Wuhan Institute of Technology, Wuhan 430205, P. R. China.

ABSTRACT: This study focuses on enhancing the photocatalytic performance of $Ti(HPO_4)_2$ for H_2O_2 synthesis. $Ti(HPO_4)_2$, an intercalated structure photocatalyst with suitable band gap energy, has great potential in photocatalytic applications. However, its performance in H_2O_2 photosynthesis needs improvement in oxygen reduction kinetics and electron lifetime. We employed oxygen vacancy engineering to modulate the local oxygen environment of $Ti(HPO_4)_2$. This process reconstructs the Ti^{3+}-O_v-P structures by leveraging push-pull electronic effects to increase the electron density at Ti^{4+} sites, thereby enhancing O_2 adsorption and activation. Moreover, we constructed an S-scheme heterojunction using WO_3 as a complementary oxidative cocatalyst. This heterojunction effectively suppressed carrier recombination and preserved the intrinsic redox abilities of each component. The optimized WO_3/TPO_v showed remarkable performance in a pure H_2O/O_2 system without sacrificial agents. It exhibited a 15-fold activity enhancement over pristine TPO and achieved an SCC efficiency of 0.75%. Our work offers a novel strategy of defect and heterojunction engineering for optimizing carrier lifetime and surface reactivity in photocatalytic systems.

KEYWORDS: $Ti(HPO_4)_2$, push-pull electronic effects, photocatalytic H_2O_2 production, S-scheme heterojunction

Received: February 11, 2025. **Revised:** May 5, 2025. **Accepted:** May 10, 2025. **Available online:** December 10, 2025
***Corresponding author:** liuyd0608@163.com (Y. Liu), h.q.jiang1119@163.com (H. Jiang), quyang@hlju.edu.cn (Y. Qu), 027wit@163.com (J. Jiang).

Graphical Abstract

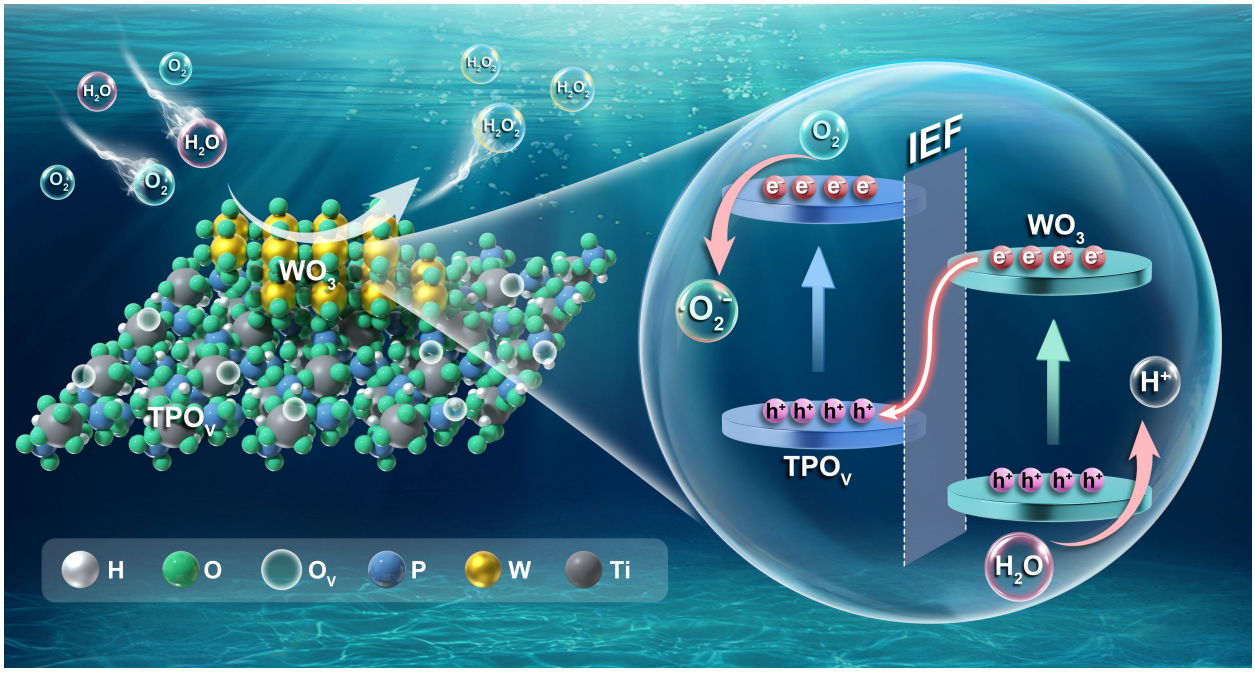

1. Introduction

Hydrogen peroxide, H_2O_2, is a versatile chemical substance that holds significant importance as an oxidizing agent, reducing agent, and bleaching agent [1-3]. Its applications span across diverse fields such as chemical industry, environmental protection, and healthcare [4-6]. Whether it is in chemical production, food processing, paper pulp bleaching, or water treatment, the demand for H_2O_2 continues to rise steadily [7-9]. However, the traditional processes for H_2O_2 production are fraught with challenges like high energy consumption, numerous side reactions, and significant risks associated with transportation and storage, which have long been pain points in the industry [10, 11]. By contrast, photocatalytic technology presents a promising and innovative alternative [12-14]. It leverages solar energy to drive photocatalytic reactions, directly converting H_2O and O_2 into H_2O_2 [15]. This process eliminates the need for high-temperature and high-pressure conditions, thereby reducing carbon emissions and environmental pollution at the source [16-18]. In other words, it achieves green chemical production in a more environmentally friendly manner [19-21]. More than that, this cutting-edge technology addresses the long-standing issue of on-site preparation and immediate application of H_2O_2 [22]. It paves the way for sustainable development and the construction of a low-carbon society by offering an eco-friendly production method.

Titanium phosphate, $Ti(HPO_4)_2$, thanks to its unique layered crystal structure and suitable band gap energy, has found extensive applications in many fields, especially in photocatalytic systems [23-27]. Currently, the generation of H_2O_2 relies primarily on two routes: the oxygen activation mechanism and the water oxidation mechanism. Because the single-electron water oxidation reaction ($H_2O + h^+ \rightarrow \cdot HO + H^+$, 2.73 V vs. NHE) exhibits extremely strong thermodynamic advantages, it is quite challenging to precisely control the reaction conditions for achieving highly selective generation of H_2O_2 via the water oxidation mechanism with water as the sole reactant [28-30]. In contrast, the oxygen activation mechanism can be further subdivided into direct oxidation and indirect oxidation mechanisms. [31]. Although the indirect oxidation mechanism must generate the thermodynamically challenging superoxide radical ($\cdot O_2^-$), its $2e^-$ tandem reaction mode enjoys distinct kinetic advantages. Additionally, the band positions of $Ti(HPO_4)_2$ are approximately −0.5 eV and +3.0 eV, which fully meets the requirement for the effective activation of O_2 [25, 26]. Therefore, using $Ti(HPO_4)_2$ as the mediator and selecting the $2e^-$ indirect oxygen activation mechanism

to synthesize H_2O_2 via photoreaction of O_2 and H_2O represents a promising candidate. Unfortunately, at present, the photocatalytic performance of $Ti(HPO_4)_2$ for H_2O_2 photosynthesis still has much room for improvement in terms of sluggish oxygen activation kinetics and short electron lifetime.

Ti^{3+} sites play a vital role in the activation of O_2, and their unique electronic structures and chemical properties enable them to exhibit positive promotional effects in numerous chemical reactions [32]. The electron spin state of Ti^{3+} sites can effectively lower the activation energy barrier of O_2 [33]. Their unpaired e^- strongly interact with the molecular orbitals of O_2 to form stable transition states. This interaction reduces the electron cloud density in the antibonding orbitals of O_2, weakens the O=O bond strength, and makes O_2 more prone to decomposition into reactive oxygen species [34, 35]. In $Ti(HPO_4)_2$, all Ti sites are present as +4-valence state, rendering the enhancement of Ti^{3+} content a critical research priority [23]. The Ti^{4+} sites in $Ti(HPO_4)_2$ are coordinated with strongly electronegative oxygen atoms (forming a Ti^{4+}-O-P configuration), where the high electronegativity of oxygen induces an electron-withdrawing effect, leaving Ti^{4+} sites in a persistent electron-deficient state. To address this, oxygen vacancy engineering can be strategically employed to modulate the local oxygen environment. By introducing oxygen vacancies (O_v), a reconstructed Ti^{3+}-O_v-P structures coordination structure is formed, which increases electron density at Ti sites by leveraging push-pull electronic effects. Simultaneously, to preserve charge neutrality, a portion of Ti^{4+} is reduced to Ti^{3+}. The newly generated Ti^{3+}-O_v-P structures not only enhance O_2 adsorption capacity and electron-donating ability (via Ti^{3+}-to-O_2 electron transfer) but also introduce impurity energy levels within the band structure. These impurity levels effectively narrow the bandgap, broaden the light absorption range, and facilitate the separation of photogenerated charge carriers [36, 37]. This dual modulation of electronic and structural properties provides a robust mechanism to optimize the photocatalytic performance of $Ti(HPO_4)_2$-based materials for applications.

A core challenge in $Ti(HPO_4)_2$ is achieving efficient charge separation while retaining strong redox capabilities. The S-scheme heterojunction offers a novel solution [38-41]. Its unique band-engineering creates an interface internal electric field and band bending, enabling electron transfer between the valence and conduction bands with weak redox potential [42, 43]. This boosts carrier separation efficiency and preserves the intrinsic redox abilities of each component: high-reduction-potential e^- in the negative conduction band and high-oxidation-potential h^+ in the positive valence band [40]. Unlike traditional II-type heterojunctions, it prevents redox capability loss. Compared to Z-scheme heterojunctions, it self-drives charge transfer without external cocatalysts or bias [44, 45]. These advantages give S-scheme heterojunctions great potential in photocatalytic applications and pave the way for new-type efficient and stable photocatalytic material systems.

Guided by the band alignment of $Ti(HPO_4)_2$, we rationally selected WO_3 as a complementary oxidative cocatalyst to construct an S-scheme heterojunction (WO/TPO_v) for photocatalytic H_2O_2 synthesis in a pure H_2O/O_2 system without sacrificial agents. The optimized WO/TPO_v exhibited a remarkable 15-fold activity enhancement over pristine TPO, achieving a solar-to-chemical conversion (SCC) efficiency of 0.75%. Oxygen vacancy engineering facilitated the generation of Ti^{3+}-O_v-P structures, which synergistically enhanced O_2 adsorption and activation. The S-scheme charge transfer pathway was confirmed to suppress carrier recombination, extending charge lifetime by 4.0-fold. Mechanistic studies combining *in-situ* spectroscopy and DFT calculations revealed a reconstructed Ti^{3+}-O_v-P structures mediated $2e^-$ indirect oxygen activation mechanism. This study pioneers a defect and heterojunction engineering strategy for synchronously optimizing carrier lifetime and surface reactivity, while establishing a robust framework for probing electron flow dynamics in complex photocatalytic systems.

2. Experimental section

2.1 Synthesis of $Ti(HPO_4)_2$ photocatalyst

In a jacketed vessel kept at 0 °C, 4 mL of titanium (IV) butoxide was introduced in a slow, dropwise fashion to 4 mL glacial acetic acid pre-diluted with 20 mL absolute ethanol, and the resulting blend was agitated for 0.5 h to afford a homogeneous stock (labelled A). Meanwhile, 6 mL orthophosphoric acid, 12 mL dilute HCl and 14 mL absolute ethanol were combined and subsequently poured into A. After 12 h of continuous stirring, the sol was decanted into a 100 mL autoclave and heated at 180 °C for 4 h. After the reaction mixture cooled to room temperature, 1.740 g of P123 was added and stirred for another 12 h until the P123 was completely dissolved. The sol was poured back into reaction kettle and subjected to secondary

heat treatment at 180 °C for 8 h. After completion of the solvothermal reaction, the solid product was collected by centrifugation, cyclically rinsed with H_2O and ethanol sequentially, and dried overnight at 80 °C. To thoroughly remove residual structure-directing agents, the powder was finally immersed in 150 mL of boiling ethanol and refluxed for 24 h. The purified product was named TPO.

2.2 Synthesis of oxygen defect $Ti(HPO_4)_2$ photocatalyst

The TPO were then placed in a tubular furnace under a hydrogen atmosphere and calcined at 400 °C for different durations (1 h, 2 h, and 3 h). After cooling to room temperature, $Ti(HPO_4)_2$ nanosheets with varying oxygen defect concentrations were obtained and named TPO_{vx}, with x representing the heat treatment time.

2.3 Synthesis of WO_3-modified oxygen defect $Ti(HPO_4)_2$ S-scheme photocatalyst

10 mmol of TPO_{v2} was dispersed in 40 mL of ethanol, and 1.5 mL of ethylene glycol was added with stirring until a clear solution formed. Then, WCl_6 was added, and the mixture was stirred until a yellow clear solution was obtained. The mixture was heated in an autoclave at 110 °C for 4 h. After cooling, the sample was centrifuged, washed, and dried to produce WO_3-modified oxygen-deficient TPO nanosheet samples named yWO/TPO_{v2}. Herein, y denotes the molar ratio of WO_3 to $Ti(HPO_4)_2$. As illustrated by the case of $3WO/TPO_{v2}$, quantification via inductively coupled plasma mass spectrometry (ICP-MS) indicated that the 100 mg/L WO/TPO_{v2} sample contained W at a concentration of 2.11 mg/L. Meanwhile, the Ti content in this identical sample was quantified as 6.86 mg/L. A visual and comprehensive depiction of the process is available in Figure 1a.

3. Results and discussion

The high-magnification electron microscopy images in Figure 1b, 1c and S1 clearly show that the $Ti(HPO_4)_2$ (TPO) samples prepared by the stepwise method exhibit highly uniform micro-morphological characteristics-ordered arrangements of uniform nanosheet structures, with statistically analyzed lateral dimensions all maintained within the range of 400±20 nm. This dimensional uniformity reflects the precise controllability of the synthetic process. When the samples undergo hydrogen reduction treatment, the obtained oxygen vacancy-rich TPO (TPO_v) material demonstrates excellent structural stability, as no obvious curling or collapse is observed at the edges of the nanosheets, indicating that the introduction of oxygen vacancies does not induce destruction of TPO crystalline structure. In the transmission electron microscopy image of Figure 1d-f, TPO_v nanosheets are uniformly decorated with WO_3 nanosheets featuring an average diameter of ~50 nm., forming a "sheet-sheet" composite structure. High-resolution TEM (Figure 1f inset) analysis reveals more detailed interfacial features: the TPO_v lamellae sheet exhibit a lattice spacing of 0.250 nm (corresponding to the (020) crystal plane), while the WO_3 nanosheets show lattice fringes of 0.260 nm (corresponding to the (202) crystal plane) [27, 46]. In the corresponding EDX elemental mapping (Figure 1g), the yellow distribution cloud of W element highly overlaps with the green cloud of Ti element in the TPO_v, further confirming the uniformity of the heterostructure. In-depth characterization data show that the introduction of oxygen vacancies has minimal impact on the intrinsic properties of TPO_v all diffraction peaks in the XRD pattern (Figure S2a) perfectly match those of α-phase $Ti(HPO_4)_2$ (JCPDS No. 83-0109), confirming the complete maintenance of the crystal phase structure [27]. The DRS spectrum (Figure S3a) reveal that there is no shift in its absorption threshold, almost identical to that of the original TPO, indicating that the optical bandgap is basically stable. For the WO/TPO_v composite material, although no characteristic diffraction peaks of WO_3 are observed in the XRD (Figure S2b) (attributed to its low loading < 5wt%), the XRD pattern of the separately prepared WO_3 sample matches with the monoclinic standard card (JCPDS No.83-0950), and the optical absorption edge (Figure S3b) also highly coincides with the theoretical value [46, 47]. Comprehensive characterization results show that this synthetic strategy successfully achieves the regulation of oxygen vacancy concentration through hydrogen reduction and the construction of uniformly distributed WO_3 nanosheets on the surface of lamellae using *in-situ* hydrothermal method without destroying the intrinsic crystal structure and optical properties of TPO. The formed heterostructure has both interfacial matching and functional synergy, providing an ideal material model for applications in photocatalysis and other fields.

For the detection of H_2O_2 production, the iodometric method was employed. As evidenced by the standard curve (Figure S4), the iodometric method demonstrated superior performance in quantifying H_2O_2 production, featuring both remarkable detection efficacy and

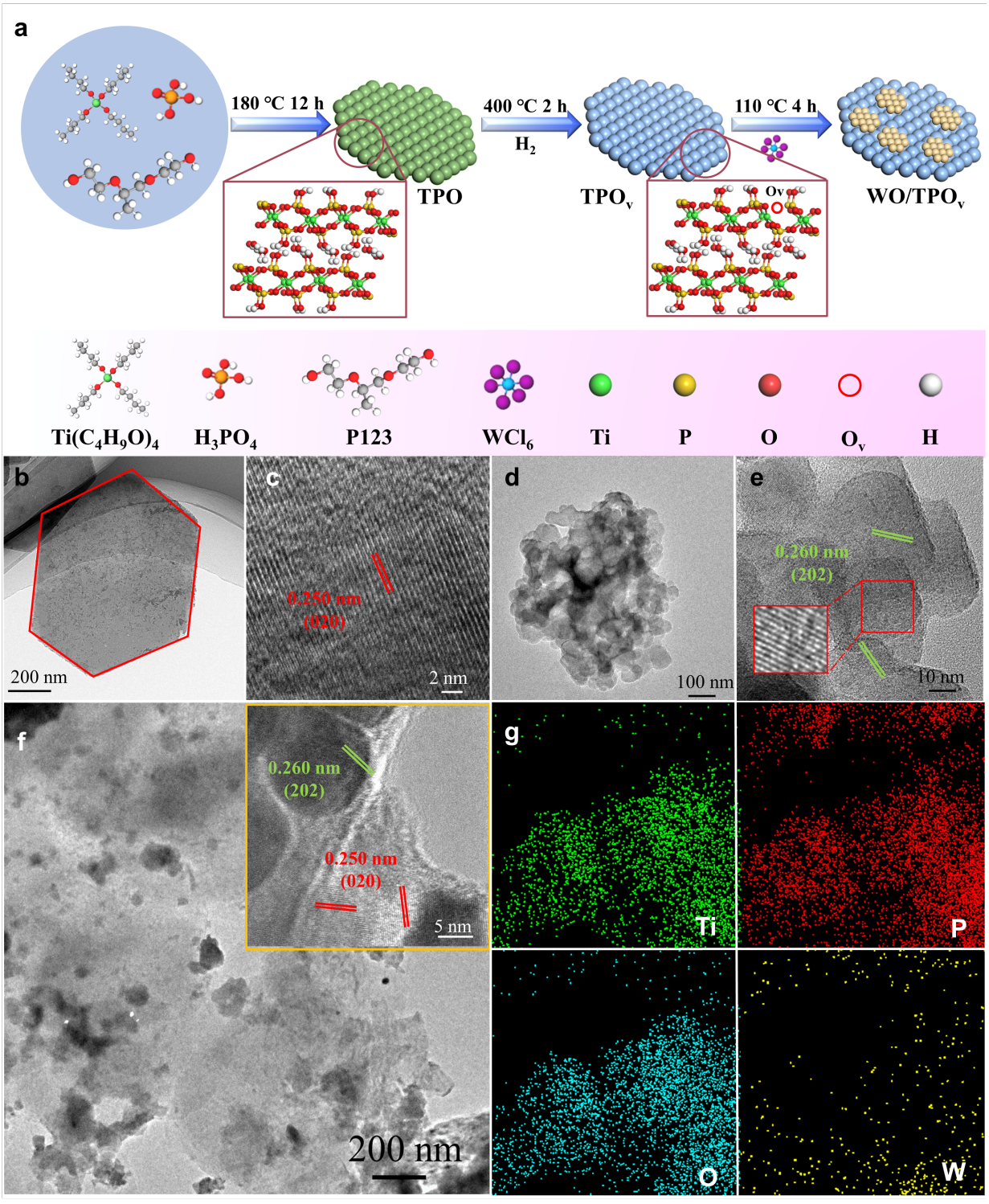

Figure 1. (a) Flowchart for the preparation of WO/TPO_v composite samples. (b) TEM and (c) HRTEM images of TPO_v. (d) TEM and (e) HRTEM images of WO. (f) TEM with HRTEM inset and (g) EDX images of WO/TPO_v.

extremely high accuracy, thus providing reliable data support for our study. With oxygen and water employed as the reactants, the photocatalytic H_2O_2 production activity achieved a leapfrog improvement

after hydrogen reduction and WO_3 modification, showing a gratifying trend of "two consecutive enhancements". Among them, the most outstanding $3WO/TPO_{v2}$ sample exhibited H_2O_2 photosynthetic performance 15-fold higher than TPO and 3.4-fold greater than TPO_{v2} (Figure 2a), fully demonstrating the critical role of the treatment process in enhancing sample performance. It should also be noted that when TPO samples were modified with the same proportion, the performance of 3WO/TPO materials increased by about 10 times compared with TPO. This indicates that when both oxygen vacancies and heterojunctions contribute to the enhancement of H_2O_2 photosynthesis, the heterojunction mechanism still plays a dominant role. Additionally, as a competitive reaction to photocatalytic H_2O_2 synthesis, the hydrogen evolution reaction was also characterized. As shown in Figure S5a, the H_2 production rate of the $3WO/TPO_{v2}$ sample with the best performance is less than 7 μmol/g/h, accounting for only about 4% of the total products. This indicates that the hydrogen evolution reaction is almost completely suppressed in this system, and photogenerated e^- are mainly directed to the $2e^-$ oxygen reduction for H_2O_2 generation rather than proton reduction for hydrogen production. This further confirms that $3WO/TPO_{v2}$ can selectively adsorb and activate O_2, thereby highly selectively driving the H_2O_2 synthesis pathway. Taking the $3WO/TPO_{v2}$ sample as an example, we conducted an in-depth evaluation of its stability during the photocatalytic reaction (Figure S5b) and basic intrinsic properties (Figure S6). After a continuous 20-hour cycle test, the H_2O_2 photosynthetic performance of this sample remained stable without obvious degradation, strongly confirming that the $3WO/TPO_{v2}$ sample possesses excellent performance recyclability and structural stability, which paves a solid way for its industrial application. More notably, the SCC efficiency of the $3WO/TPO_{v2}$ sample peaked at 0.75% (Figure 2b), which is a remarkable level in the field of photocatalysis. When using SCC efficiency as the evaluation index for the H_2O_2 photosynthetic performance of photocatalysts, $3WO/TPO_{v2}$ even outperformed most relevant photocatalysts documented recently under comparable experimental conditions (Figure 2c and Table S1), making it stand out among numerous photocatalysts and demonstrating great application potential.

The process of photocatalytic H_2O_2 production is considered a complex dynamic process involving two competing steps: H_2O_2 generation and H_2O_2 decomposition. Given that H_2O_2 may react with the e^- or h^+, leading to further decomposition of the generated H_2O_2, we deeply investigated the H_2O_2 degradation behavior of tested photocatalysts including TPO, TPO_v, WO_3, and WO/TPO_v. As is evident from Figure S7, tested materials presented low H_2O_2 degradation activity, suggesting that H_2O_2 maintains excellent stability and is not prone to decomposition, thus providing a strong guarantee for the effective accumulation of H_2O_2. For the purpose of thoroughly investigating this dynamic H_2O_2 transformation process, we accurately calculated the H_2O_2 generation rate constant (K_f) and decomposition rate constant (K_d) based on the data in Figure S7, where K_f adheres to zero-order reaction kinetics, while K_d follows first-order reaction kinetics. As distinctly revealed in Figure 2d, WO/TPO_v not only had the minimum K_d, which reflects its excellent performance in inhibiting H_2O_2 decomposition, but also possessed the maximum K_f, implying its significant advantage in promoting H_2O_2 generation. These two outstanding performances collectively confirm that the WO/TPO_v composite material exhibits the best photocatalytic H_2O_2 activity, holding great application value in the field of photocatalytic H_2O_2 production.

Furthermore, we conducted an $H_2{}^{18}O$ isotope experiment (Figure 2e) under identical conditions to $H_2{}^{16}O$. Luminol was introduced as a probe into the photoreaction system to trace the origin of H_2O_2 generated over $3WO/TPO_{v2}$. Upon adding luminol solution and horseradish peroxidase (HRP) into the $3WO/TPO_{v2}$ suspension under light irradiation, an isotope peak corresponding to luminol oxide-^{16}O was detected, accompanied by a weaker peak for luminol oxide-^{18}O. This result strongly confirms that the as-synthesized H_2O_2 is predominantly derived from O_2 reduction, elucidating the core pathway for photosynthesis H_2O_2. To further validate the above conclusions, we investigated the effects of various factors on H_2O_2 photosynthesis (Figure 2f) [48-50]. The experiments showed that H_2O_2 was not produced in the system when light or photocatalyst was absent, fully demonstrating that light and photocatalyst are two indispensable key factors for H_2O_2 photosynthesis. Additionally, if the H_2O_2 photosynthetic process in the WO/TPO_v system fully followed the oxygen activation mechanism, then the H_2O_2 photosynthetic performance would have decreased by approximately 80% and 100% when O_2 was replaced. This is significantly higher than the experimental results, which were 70% and 92%, respectively. This clearly indicates that although the oxygen activation mechanism serves a pivotal function during the H_2O_2 generation process, there are still other auxiliary H_2O_2 photosynthetic pathways, and the contribution of the water activation

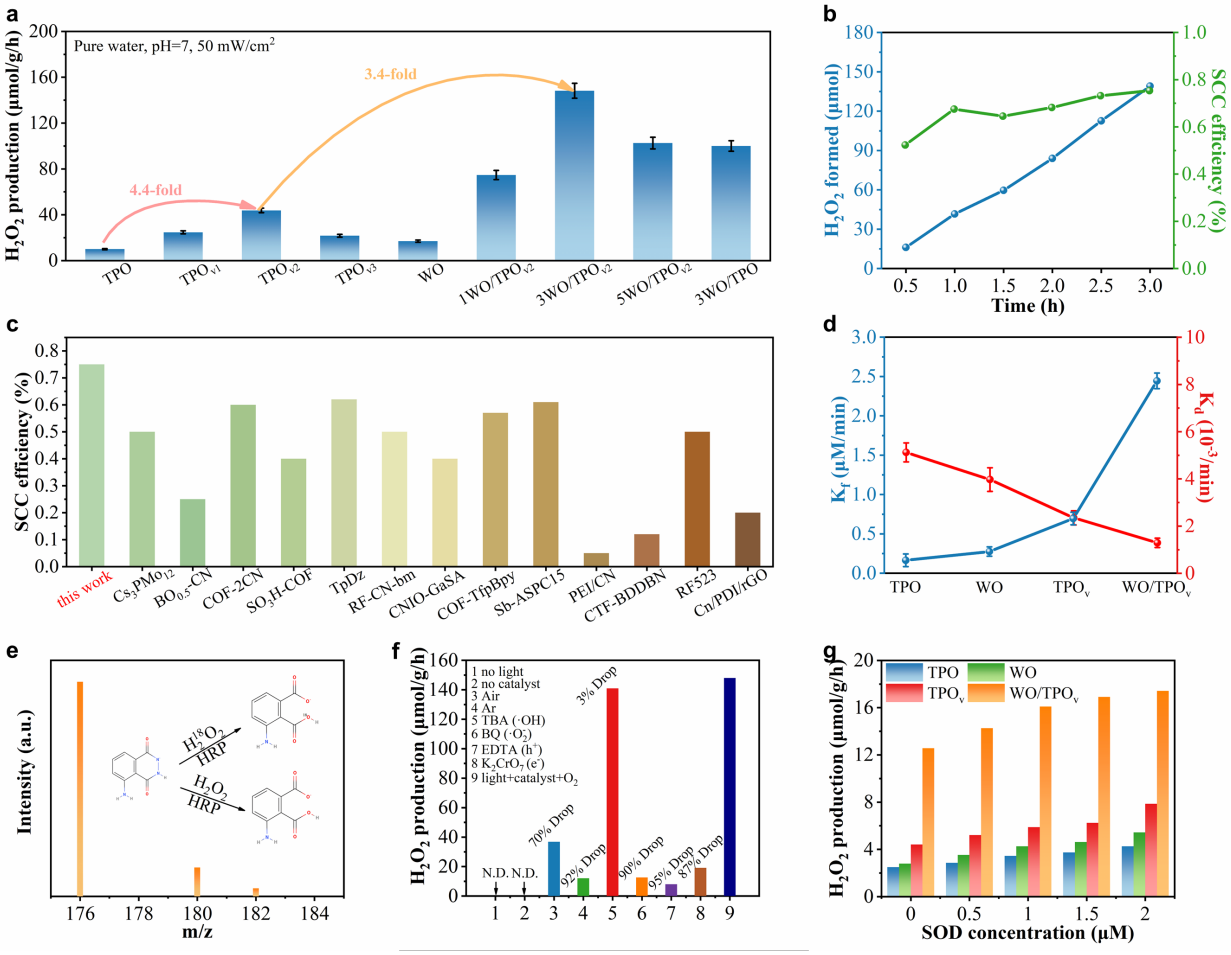

Figure 2. (a) Photocatalytic performance of different samples towards H_2O_2 production with pure water under light irradiation of 1h. (b) H_2O_2 yields and SCC efficiencies of WO/TPO_v under simulated sunlight irradiation. (c) Comparison of the SCC efficiencies of WO/TPO_v and relevant materials. (d) The H_2O_2 formation rate constant (K_f) and decomposition rate constant (K_d) corresponding to tested catalysts. (e) Mass spectra of luminol oxidized by H_2O_2 produced via photocatalytic reactions with $H_2{}^{18}O$ over WO/TPO_v. (f) H_2O_2 generation efficiencies of the tested samples under varying gas conditions or distinct sacrificial agents under light irradiation of 1h. (g) H_2O_2 production rates of tested materials at varying superoxide dismutase (SOD) concentrations under light irradiation of 1h.

mechanism to H_2O_2 photosynthetic performance is about 8%. The analysis of the effects of various radicals revealed that the impact of ·OH on H_2O_2 photosynthesis is relatively minor, indicating that the reaction pathway for H_2O_2 formation via ·OH coupling hardly occurs. Considering the combined effects of e^- and $\cdot O_2^-$, the changes in H_2O_2 photosynthetic performance after capturing these two species show essential consistency, suggesting that e^- almost entirely follow the tandem reaction pathway of $O_2 + e^- \rightarrow \cdot O_2^-$, $\cdot O_2^- + e^- + H^+ \rightarrow H_2O_2$. Most importantly, after quenching h^+ in the system, the H_2O_2 photosynthetic performance plummeted sharply. In conjunction with the changes in performance due to gas replacement, we can determine that the direct activation of water by h^+ to produce H_2O_2 accounts for 5% of the total performance, while more h^+ is used to oxidize water to supply H^+ for the oxygen activation mechanism to produce H_2O_2. This finding provides a key clue for our in-depth understanding of the mechanism of photocatalytic H_2O_2 production. To further explore the role of $\cdot O_2^-$ in the H_2O_2 photosynthetic process, we used nitroblue tetrazolium (NBT, Figure S8) to verify the oxygen activation capability and superoxide dismutase (SOD, Figure 2g) to investigate the accelerating effect of $\cdot O_2^-$ on H_2O_2 photosynthetic performance [51, 52]. The experimental results corroborated the aforementioned conclusions, thus confirming that $\cdot O_2^-$ generation exerts a decisive effect on boosting photocatalytic H_2O_2 synthesis and is one of

the core factors for achieving efficient photocatalytic H_2O_2 production.

Efficient charge transfer mechanisms are crucial for enhancing material performance. We focus on the heterojunction of TPO_v and WO. Through a series of rigorous and comprehensive experiments and analyses, we explore its unique charge transfer pathway. Using two characterization methods (Figure S9), the band positions of TPO_v and WO were precisely quantified. As shown in the results, the band positions of TPO_v range from -0.48 V to 2.93 V, while those of WO ranges from 0.13 V to 3.19 V. These two sets of data indicate that the band positions of TPO_v and WO are staggered. This unique band structure provides an essential basis for the S-scheme charge transfer mechanism [53-55].

To gain deeper insight into the S-scheme charge transfer pathway of WO/TPO_v, we designed a series of XPS detection experiments (Figure 3a-c, Figure S10). Among the detection results of many elements, the data of Ti 2p, P 2p and W 4f are the most prominent. After the formation of the heterojunction, the binding energies of Ti and P, the two key elements of TPO_v, show a significant positive shift. This is attributed to the lower work function and higher Fermi level of TPO_v (Figure S11). Per semiconductor physics principles, electron transfer occurs from TPO_v to WO upon their contact, accompanied by an opposite trend in the W 4f binding energy. Fermi level alignment between the two semiconductors following contact induces band bending in both materials. The bending of the energy band promotes the interaction and recombination between the e^- of WO and the h^+ of TPO_v, and constructs the depletion region and accumulation region of e^- at the heterojunction interface, so that WO is negatively charged and TPO_v is positively charged, so as to establish the built-in electric field (BIEF) between them. This BIEF plays a key function in enhancing the separation efficiency and accelerating the carriers transfer, and is the key factor

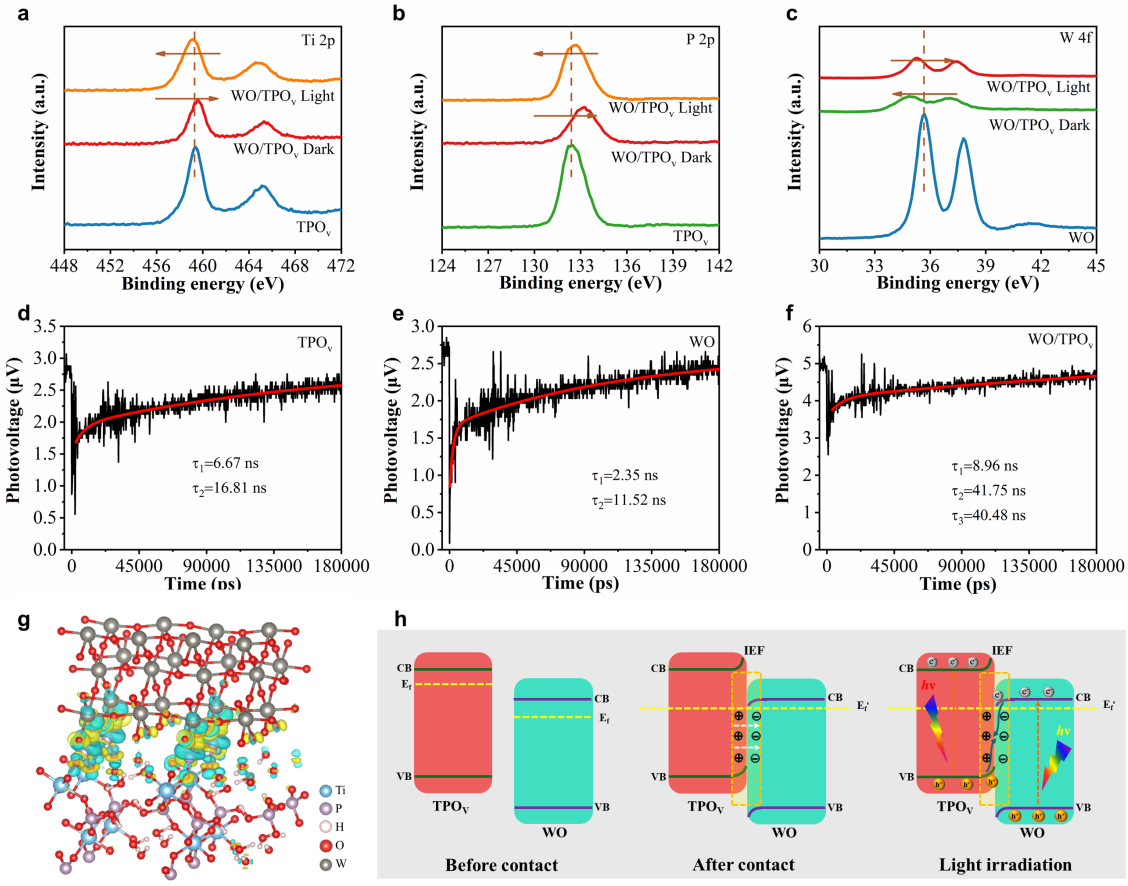

Figure 3. XPS spectra of (a) Ti 2p and (b) P 2p for TPO_v and WO/TPO_v, and (c) W 4f for WO and WO/TPO_v. TPV spectra corresponding to (d) TPO_{v2}, (e) WO, and (f) 3WO/TPO_{v2}. (g) Electron density differences for WO/TPO_v heterojunction. (h) The formation of advantage sample S-scheme heterojunction, and the proposed charge transfer and separation mechanism.

to achieve efficient charge transfer. When WO/TPO_v is exposed to light, the BIEF induces the directional transfer of e^- from WO to TPO_v, which is corroborated by the inverse shifts in the XPS spectra of Ti 2p, P 2p, and W 4f. This achieves the directional migration of photogenerated charges following the S-scheme charge transfer mechanism [56-58].

Transient photovoltage spectroscopy is a key means to explore the photogenerated charge separation characteristics of materials. In-depth analysis of TPV spectra via detailed exponential fitting facilitates the extraction of charge lifetime information during different separation processes [59-61]. In the fitting process, τ_1 is mainly used to describe the life of the charge initial separation stage, which reflects the initial dynamic process of the separation of photogenerated electron hole pairs. For a single photocatalyst system, τ_2 reflects the material surface charge life, that involves many factors such as the recombination and transfer of charge on the surface and interaction with surface defect states. In the composite photocatalyst, τ_2 more reflects the charges directional transfer between material interfaces, which is affected by many factors, such as material band matching, interface contact quality and BIEF. As for τ_3, it mainly appears in the composite photocatalyst system to reflect the effective life of photogenerated charge on the material surface. Based on the comprehensive experimental results systematically presented in Figure 3d-f, both TPO_v and WO exhibit distinct dynamic characteristics that are well consistent with the mathematical model of a second-order exponential equation, further confirming their similar charge carrier relaxation behaviors. This indicates that charge dynamics are relatively straightforward, primarily involving charge intrinsic separation in the bulk phase and subsequent diffusion on the surface. During the intrinsic separation process, photogenerated electron hole pairs begin to separate under the effect of electric field or carrier concentration gradient in the material, forming free moving carriers. In the process of surface diffusion, these carriers diffuse near the surface of the material until they are combined or captured by the active sites on the surface. However, in the WO/TPO_v heterojunction system, the effective lifetime of photogenerated charge is significantly prolonged, showing the characteristics of third-order exponential equation, in which τ_3 is as high as 40.48 ns. This significant result underscores the existence of a highly efficient charge transfer mechanism in the heterojunction system. When the photogenerated charge is formed at the interface of the heterojunction, the BIEF will induce the photogenerated e^- to migrate from one material to another, while the h^+ migrate in the opposite direction. This oriented charge transfer effectively suppresses charge recombination, prolongs carrier lifetime, and significantly elevates charge separation efficiency, thus offering ample active carriers to drive photocatalytic reactions, which is expected to improve the performance of photocatalysts in practical applications. Through exponential fitting of TPV spectra and systematic investigation of the energy band position relationship in the WO/TPO_v composite, researchers elaborately plotted the τ-corresponding charge transport pathway diagram (Figure S12). The schematic diagram shows in detail the transmission path and law of photo generated charge in the heterojunction in an intuitive form. By observing the schematic diagram, we can clearly see how the photogenerated charge in the heterojunction is affected by the BIEF and migrates and separates along a specific path. For example, photogenerated e^- migrate rapidly from WO to TPO_v driven by the BIEF, while h^+ remain on the surface of WO.

Beyond the experimental investigations discussed above, for a better understanding of the S-scheme mechanism of WO/TPO_v composite from the theoretical level, based on the accurate characterization of chemical states of interface elements by *in-situ* XPS and the real-time monitoring results of photogenerated charge dynamics by transient photovoltage spectroscopy, we used the method of combining first principles calculation with density functional theory (DFT) to systematically simulate the charge transfer direction of heterojunction interface (Figure 3g and Figure S13 for relevant data). In the calculation process, we constructed an atomic model including different interface bonding modes, and quantitatively analyzed the charge density distribution before and after the formation of the heterojunction by accurately solving the electronic structure equation [62, 63]. The calculation results show that the WO charge density at the interface increases remarkably when TPO_v and WO form a heterojunction by chemical bonding. This charge redistribution phenomenon is highly consistent with the valence state changes of elements observed *in-situ* XPS experiments. This theoretical calculation result not only verifies the experimental conclusion from the electronic structure level, but also reveals the essence of charge transfer driven by the Fermi level flattening effect-under the action of thermodynamic equilibrium, the e^- with higher energy in TPO_v will spontaneously diffuse to WO until the Fermi levels align. According to the multi-faceted experimental characterization results and theoretical computation outcomes, we systematically constructed a

comprehensive schematic diagram of the formation mechanism of the BIEF and the electron-hole transport behavior during the formation of the WO/TPO_v composite (Figure 3h). The schematic diagram shows in detail the whole process from the formation of chemical bonds at the interface of heterojunction, the charge diffusion caused by Fermi level alignment, owing to the formation of the BIEF and driving the directional migration of photogenerated carriers.

To investigate the dynamic charge transfer mechanism in WO/TPO_v, we conducted femtosecond transient absorption (fs-TA) spectroscopy measurements under an excitation wavelength of 320 nm. The negative ΔA signal observed at 400-500 nm signifies ground-state bleaching (GSB), reflecting the depletion of ground-state e^- upon photoexcitation (Figure 4a and Figure 4d). As the detection time increases, the TA intensity of the TPO_v and WO/TPO_v catalysts decreases significantly (Figure 4b and Figure 4e). When the detection time is further extended, the TA intensity of the TPO_v and WO/TPO_v catalyst increases significantly. This is because the h^+ capture the photogenerated carriers, shortening the lifetime of the initial excited state, resulting in rapid decay of the TA signal. These results indicate that the recombination rate of photoexcited charges in WO/TPO_v is effectively suppressed through a new channel, leading to the accumulation of photoexcited charges in the CB and VB, respectively. Combined with the results of *in-situ* XPS, it can be inferred that the photoexcited e^- of WO are efficiently transferred to TPO_v via the strong IEF between WO and TPO_v. This transfer process promotes the utilization of photoexcited charges in WO/TPO_v. The normalized dynamic kinetic decay curves at 400 nm and their fitting results with a three-exponential decay function are shown in Figures 4c and 4f. The decay process typically includes three stages: ultrafast electron diffusion, electron trapping, and recombination of e^- with unconsumed h^+. TPO_v exhibited longer electron diffusion (τ_1 = 1.39 ps) and trapping processes (τ_2 = 22.95 ps) compared to WO/TPO_v. Both τ_1 and τ_2 of WO/TPO_v were reduced, indicating faster electron dynamics and shorter time required for diffusion and trapping processes. These findings confirm that in the WO/TPO_v heterojunction, after the generation of photoexcited e^- by WO and TPO_v, most e^- in the CB of WO are efficiently and ultrafastly transferred to the VB of TPO_v under the action of the strong IEF. This rapid electron transfer reduces diffusion and trapping, thereby extending the separation time of photoexcited charges. This directly verifies the advantage of the built-in IEF in the WO/TPO_v heterojunction for efficient photogenerated charge transfer and separation, allowing high concentrations of photoexcited charges to be retained in WO/TPO_v, respectively.

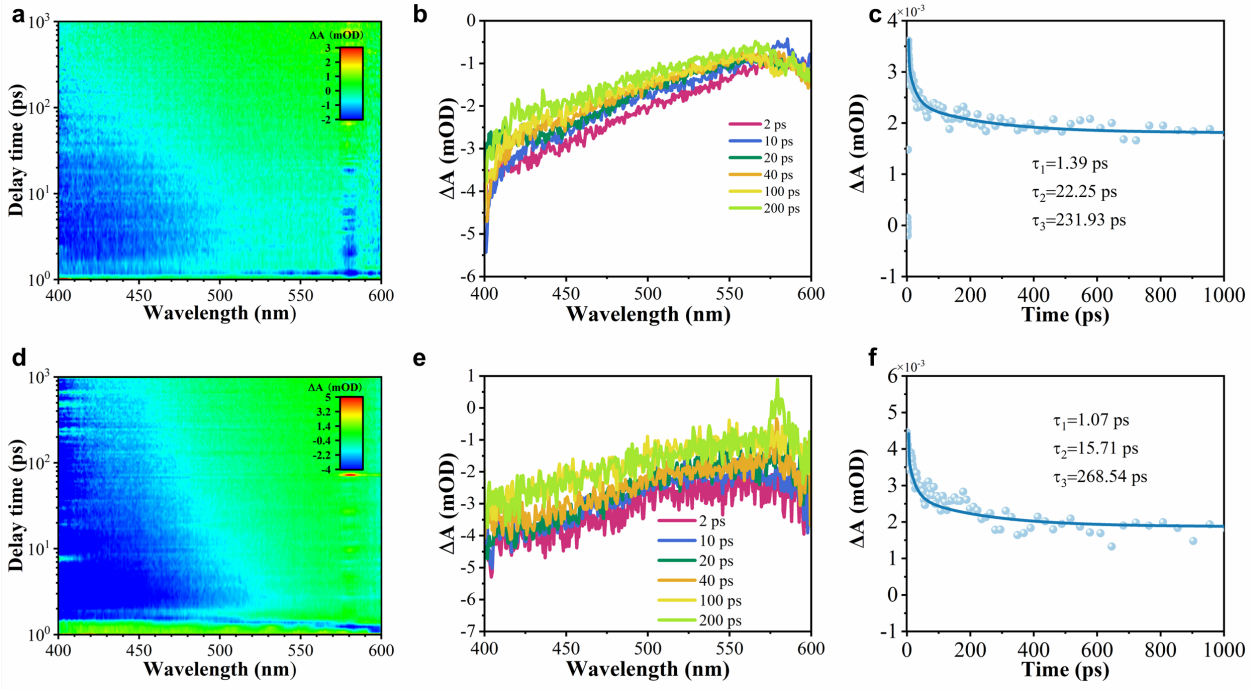

Figure 4. 2D pseudo-color maps of fs-TA spectra (a and d), transient fs-TA spectra (b and e), and kinetic time profiles (c and f) of normalized transient absorption at 400 nm, in TPO_v, and WO/TPO_v under 320 nm laser pulse irradiation.

In order to further consolidate the theoretical basis of the S-scheme mechanism in WO/TPO_v heterostructures, we designed and implemented a multi-dimensional supplementary experimental system. A single wavelength laser generator was used as the light source to select six representative wavelengths for photocurrent testing of single component (TPO_v and WO) and composite material (WO/TPO_v) (Figure S14), the optical response characteristics of WO and TPO_v semiconductors were systematically studied by accurately adjusting the excitation wavelength. The experimental data show that when the excitation wavelength only meets the optical absorption threshold of a single component of WO or TPO_v, the photocurrent density remains at a low level. When the excitation wavelength meets the optical excitation conditions of WO and TPO_v at the same time, the current density of the heterojunction system shows an exponential jump, which is highly consistent with the efficient charge separation process caused by the two-component cooperative excitation in the S-scheme electron-hole transport mechanism. Through the utilization of *in-situ* EPR test (Figure S15 and S16), we captured the migration path of photogenerated carriers. Based on the accurate calculation of the energy band position, $O_2/\cdot O_2^-$ and -OH/·OH oxidation-reduction potential of WO and TPO_v, combined with the dynamic changes of the characteristic spin adduct signal in the EPR spectrum, the directional migration characteristics of e^- at the heterojunction interface were confirmed [64, 65]. The results show that under the condition of light excitation, the h^+ generated by the valence band of TPO_v and the e^- generated by the conduction band of WO pass through the S-scheme charge transmission path, which realizes the efficient charge separation and redistribution, and finally makes the photogenerated e^- specifically enriched in the conduction band level of TPO_v. Figure S17 shows the excellent performance of WO/TPO_v heterojunction driven by S-scheme mechanism from the three dimensions. Photophysical tests revealed the ultrafast kinetic process of charge transfer at the interface. Photoelectrochemical tests verified the linear relationship between charge separation efficiency and photocurrent response, while photochemical experiments directly showed the high activity and durability of the heterojunction in the photocatalytic reaction. The experimental results not only provide comprehensive verification of the S-scheme mechanism but also fully demonstrate that the WO/TPO_v heterojunction possesses excellent charge separation capability under this charge transfer pathway.

In the present work, systematic experimental and theoretical investigations have validated that photoexcited e^- tend to accumulate preferentially on the conduction band of TPO_v. Notably, these photoexcited e^- serve as the predominant active species responsible for the photosynthesis of H_2O_2 within the WO/TPO_v photocatalytic system. Consequently, deciphering the specific activation mechanism of the spatially separated photogenerated e^- is indispensable for gaining comprehensive insights into the fundamental origins of the overall photocatalytic process. To this end, an XPS experiment was designed to study the performance of hydrogen reduction in the composite system to reveal the influence of the oxygen vacancy structure on the surface electronic structure of the material. By comparing the XPS spectra of TPO and TPO_v (Figure 5a and Figure S18), a distinct new characteristic peak of binding energy was observed on the surface of the TPO_v catalyst, with its position centered at approximately 532 eV. This characteristic peak is ascribed to O_2 molecules adsorbed on oxygen vacancies, indicating that many oxygen vacancies are generated in TPO material after hydrogen reduction treatment. Analysis of the O 1s XPS spectra (Figure S18a) reveals a monotonic increase in oxygen-vacancy content with prolonged H_2 treatment: rising from 7.2% in pristine TPO to 17.2% (TPO_{v1}), 34.4% (TPO_{v2}), and ultimately 39.1% (TPO_{v3}), unequivocally confirming H_2 thermal reduction as a direct route for generating oxygen vacancies. Further analysis showed that in TPO_v material, the content of Ti^{3+} binding energy characteristic peaks (located at 458.59 eV and 464.26 eV) significantly increased, and the binding energy of these peaks slightly shifted to the negative direction. This phenomenon can be attributed to the formation of oxygen vacancies in the Ti-O-P structure, leading to the reconstruction of the Ti^{3+}-O_v-P structure [66, 67]. By virtue of the oxygen atom deficiency, the intense electronegative coordination interaction exerted by oxygen atoms to captivate e^- is diminished, which in turn elevates the electron density of Ti sites. More importantly, the charge compensation mechanism also promotes the partial reduction of Ti^{4+} sites to Ti^{3+} sites, further enhancing the electronic activity of the material. In order to further corroborate the presence of Ti^{3+} active sites in the TPO_v catalyst, low-temperature EPR spectroscopic measurements were performed (Figure 5b). Systematic characterization results revealed the presence of distinct Ti^{3+} species signals in the TPO_v catalyst, where the associated g-values were determined to be 1.93, 1.99, and 1.998 [68, 69]. The presence of these signals further confirmed that the introduction of oxygen vacancies indeed promoted the generation of Ti^{3+} sites. The restructured Ti^{3+}-O_v-P

structure may become the active center for photogenerated e^-, thereby improving the photocatalytic performance of the material. To gain deeper insights into the variations in charge density subsequent to the generation of the restructured Ti^{3+}-O_v-P structure, theoretical calculations were performed on TPO and TPO_v (Figure 5c and Figure S19-20). The calculation results showed that the atomic charge density adjacent to oxygen vacancies increased. This finding further validated that following the elimination of oxygen atoms, the electron density at Ti sites is augmented owing to the scarcity of electron-withdrawing capacity. Such an elevation in electron density facilitates the sequestration and activation of photoexcited e^-, thereby improving the efficiency of the WO/TPO_v catalyst system in H_2O_2 photosynthesis.

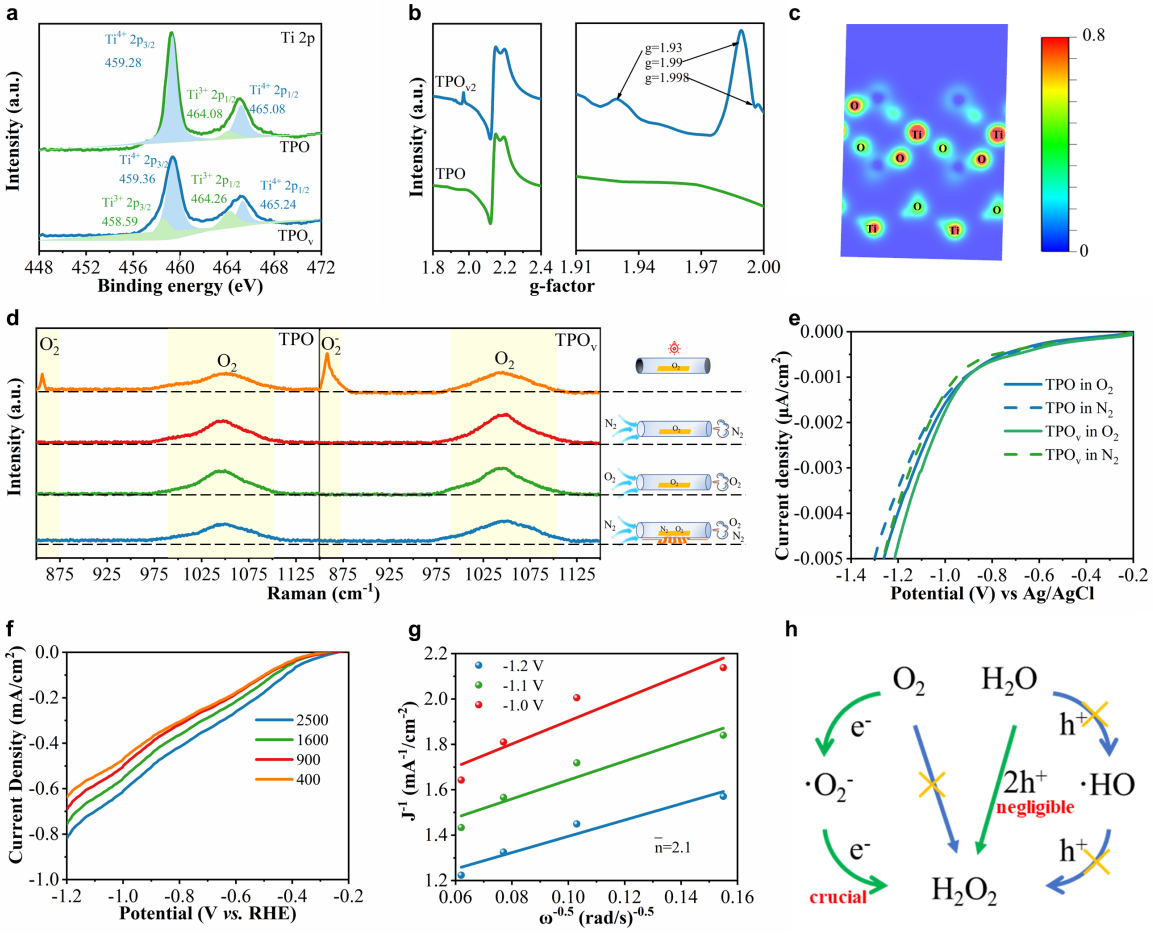

Figure 5. (a) XPS spectra of Ti 2p and (b) EPR spectra of TPO and TPO_v. (c) Local charge density map of TPO_v. (d) *In-situ* Raman spectra and (e) electrochemical reduction curves in different atmosphere of TPO and TPO_v. (f) The Linear-sweep voltammograms signal of WO/TPO_v catalyst measured on a rotating disk electrode at different rotation speeds. (g) K-L plots of WO/TPO_v catalyst at constant electrode potentials. (h) Validated pathways for photocatalytic H_2O_2 production.

To deeply investigate the impact of the Ti^{3+}-O_v-P structure on the O_2 activation effect, we first systematically examined its O_2 adsorption capacity. By analyzing the data in Figures S21 and S22, we found that in the TPO_v catalyst, with the extension of O_2 adsorption duration, the characteristic binding energy peak corresponding to adsorbed oxygen in the in-situ O1s XPS spectrum has been significantly higher than the corresponding peak of the TPO catalyst since the initial stage of the experiment, indicating that the TPO_v catalyst possesses a stronger O_2 adsorption activity. Further O_2-TPD experimental results also confirmed this point [70-72]. Whether considering chemisorption or physisorption, the O_2 adsorption activity of the TPO_v catalyst is significantly better than that of the TPO material. These findings lay a solid foundation for subsequent O_2 activation capacity testing. Prior to the formal *in-situ* Raman spectroscopy measurements, a

series of pretreatment operations were conducted, encompassing the elimination of surface contaminants, adsorption of O_2, and purging with N_2 to ensure the reliability of subsequent test results. As illustrated in Figure 5d, the Raman spectrum reveals that the characteristic Raman peak assigned to adsorbed O_2 remains essentially unchanged for the same material throughout the entire testing period, confirming the absence of free O_2 interference during detection [73-75]. Furthermore, the intensity of the adsorbed oxygen-related Raman peak for TPO_v is consistently higher than TPO, which further verifies that the Ti^{3+}-O_v-P structure enhances the O_2 adsorption capability. Notably, upon introducing light into the monitoring system, TPO_v exhibits a more prominent $\cdot O_2^-$ characteristic peak, indicative of its superior oxygen activation performance. This finding is corroborated from an alternative perspective via atmosphere-controlled electrochemical oxygen reduction measurements (Figure 5e). Upon switching the purge gas from N_2 to fully O_2-saturated electrolyte, the potential required to activate O_2 on TPO_v material dropped markedly below that observed for TPO material. In addition, the SS-SPS spectra with different atmospheres (Figure S23) and DMPO-$\cdot O_2^-$ EPR spectrum (Figure S24) also provided evidence supporting this conclusion. From the perspective of electronic structure essence, the projected density of states clearly reveals the decisive regulatory role of oxygen vacancies (O_V) in the catalytic activity of TPO (Fig. S25). For the vacancy-free sample, the density of states near the Fermi level (E_f) is almost vacant with a wide band gap. The Ti 3d and O 2p orbitals are locally confined, failing to provide sufficient e^- to the O_2 π^* orbitals, thus oxygen activation is restricted by the electron transfer prohibition. After the introduction of oxygen vacancies, to strictly maintain the overall electrical neutrality of the material, the positive charge defects released by oxygen vacancy formation trigger a local charge self-compensation mechanism. Under the action of this mechanism, Ti^{4+} ions adjacent to the oxygen vacancies are selectively occupied by e^- and reduced to Ti^{3+}, thereby forming a local polaron state with high electron density in the defect region, and the $3d^1$ e^- form new energy levels within the band gap. These levels rehybridize with the relaxed O 2p orbitals around the vacancies, generating continuous defect states with high intensity near E_f. Such defect states simultaneously satisfy three electronic criteria for oxygen activation: (1) The density of states crosses E_f, enabling immediate participation of e^- in the reaction; (2) The significant overlap between Ti 3d and O 2p peaks achieves effective coupling with the O_2 π^* orbitals; (3) The significant increase in the density of states at E_f, greatly enhancing the electron supply capacity. The experimentally observed enhancement in oxygen activation activity is thereby directly explained at the electronic structure level. In summary, through a series of experiments, we have demonstrated that the Ti^{3+}-O_v-P structure has significant advantages in O_2 adsorption and activation.

In this study, the rotating disk electrode technique was adopted to quantify the selectivity of O_2 activation [76-79]. Measurements were repeated at four precisely controlled rotation speeds: 400, 900, 1600 and 2500 rpm, to generate a set of hydrodynamic profiles. The resulting current-potential data were used to calculate the electron-transfer number, allowing the $2e^-$ versus $4e^-$ selectivity of the O_2 activation process to be evaluated under well-defined mass-transport conditions. The current density data obtained under these different rotation speed conditions, as shown in Figure 5f, provided important experimental evidence for analyzing the O_2 activation process. Furthermore, we conducted an in-depth analysis of the experimental data using the Koutecky-Levich (K-L) theory and plotted the K-L graph shown in Figure 5g [80]. This graph clearly illustrates the average electron transfer number (n) during the O_2 reduction process. For the WO/TPO_v catalyst, the averaged n-value is 2.1, which is highly consistent with the theoretical $2e^-$ O_2 reduction mechanism. More importantly, the selectivity of this material during the O_2 reduction step is as high as 95.2%, fully demonstrating that the WO/TPO_v composite material primarily follows the $2e^-$ indirect O_2 activation pathway. Based on the analysis results of the averaged n-value together with the mechanistic evidence provided by trapping experiments (as shown in Figure 2f), we further plotted the H_2O_2 generation mechanism diagram based on the indirect $2e^-$ O_2 activation pathway, as shown in Figure 5h. The diagram provides an end-to-end mechanistic portrait of O_2-to- H_2O_2 conversion via the indirect $2e^-$ mechanism under the catalysis of the WO/TPO_v composite material.

A deep understanding of molecular behavior during photocatalytic reactions is crucial for elucidating reaction mechanisms and optimizing catalyst design. In the previous section, we systematically investigated the adsorption capacity and active sites of the WO/TPO_v heterojunction toward O_2. Building on that, this section employs *in-situ* DRIFTS to study the key reaction steps during the photocatalytic H_2O_2 synthesis process $O_v$er the WO/TPO_v heterojunction, with a particular focus on the adsorption behavior of H_2O molecules and the formation of H_2O_2 (see Figures S26-

27 and 6a-c). In the range of 3100-3700 cm^{-1}, a characteristic infrared band assignable to the O-H stretching mode of adsorbed H_2O can be clearly identified [81-83]. The intensity of these peaks reflects the adsorption capacity of the catalyst surface toward H_2O. Under identical experimental conditions, we compared three representative catalyst samples: TPO, TPO_v, and WO/TPO_v. The results showed that the intensities of the H_2O characteristic peaks were nearly identical across all three samples, indicating that their H_2O adsorption capacities are similar. This suggests that neither the introduction of oxygen vacancies (O_v) and Ti^{3+} sites to form the Ti^{3+}-O_v-P structure nor the incorporation of WO to construct the heterojunction interface significantly alters the surface adsorption behavior of H_2O molecules. This finding implies that the activation of H_2O molecules may not be the key factor contributing to the enhanced photocatalytic performance in this system. Instead, combined with our previous analysis of O_2 adsorption behavior, it is reasonable to infer that the improved H_2O_2 synthesis performance is primarily due to the effective adsorption and activation of O_2 molecules. To verify this hypothesis, we further monitored the infrared signal changes during H_2O_2 formation. In the range of 2840-2860 cm^{-1}, characteristic infrared absorption peaks attributed to H_2O_2 molecules were observed (Figure 6b) [84, 85]. The appearance of these peaks directly reflects the formation of H_2O_2 on the catalyst surface. Under the same reaction conditions, the intensities of the H_2O_2 characteristic peaks followed the order: WO/TPO_v > TPO_v > TPO, which is consistent with their photocatalytic activities in H_2O_2 synthesis. This further confirms that structural optimization of the catalyst promotes H_2O_2 formation efficiency.

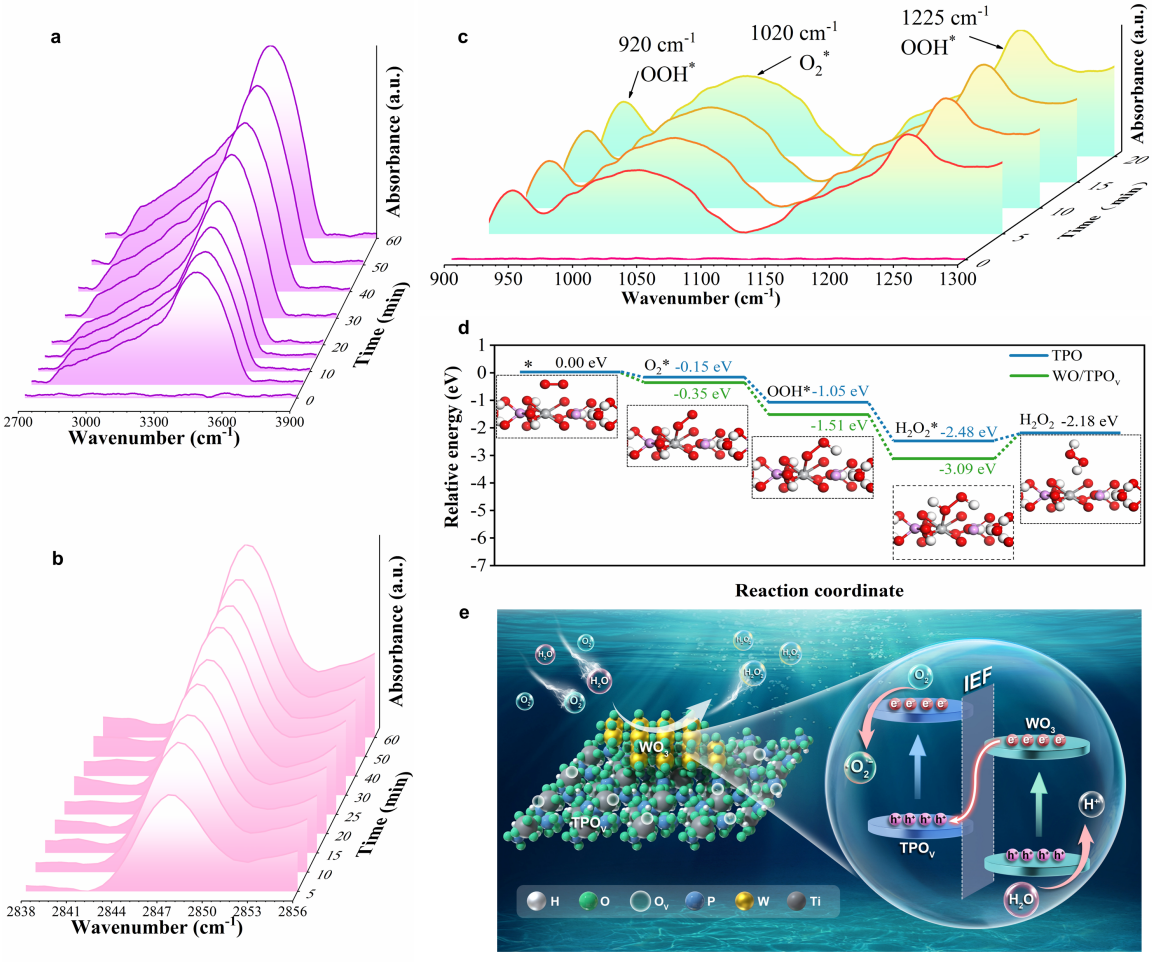

Figure 6. *In-situ* DRIFTS of (a) H_2O adsorption, (b) H_2O_2 production and (c) H_2O conversion on WO/TPO_v catalyst. (d) Free energy diagrams for H_2O_2 production processes over WO/TPO_v catalyst with optimized configurations for each step. (e) Schematic of the S-scheme mechanism and H_2O_2 photosynthesis reaction involved in WO/TPO_v catalyst.

Beyond macroscopic observations of H_2O adsorption and H_2O_2 formation, we also focused on the microscopic pathway of the stepwise conversion of O_2 and H_2O into H_2O_2. As shown in Figure 6c, with increasing illumination time, the characteristic peaks of O_2* and OOH* radicals progressively intensified [86-88]. Compared with substrate, the WO/TPO_v catalyst exhibited a pronounced surge in the signal intensities of both radical species. This experimental evidence strongly supports that the Ti^{3+}-O_v-P structure and the introduction of WO act as a vital facilitator in accelerating O_2 activation and promoting H_2O_2 photosynthesis. On the basis of *in-situ* DRIFTS results, we further employed DFT to investigate the Gibbs free energy changes of the indirect $2e^-$ O_2 reduction mechanism on TPO and WO/TPO_v [89-91]. As shown in Figure 6d, all theoretical models exhibited a downward trend in Gibbs free energy along the reaction pathway, indicating that H_2O_2 formation is thermodynamically feasible on TPO-based photocatalysts. More importantly, at each key stage-O_2 adsorption, OOH* formation, and H_2O_2 generation-the Gibbs free energy values for WO/TPO_v were significantly lower than those for pure TPO. This is mainly due to the strong O_2 adsorption capability of the reconstructed Ti^{3+}-O_v-P structure, which effectively captures and activates O_2 molecules, facilitating subsequent reactions. In the indirect $2e^-$ O_2 activation mechanism, the formation of the OOH* intermediate and its protonation to H_2O_2 are generally considered the rate-determining steps, directly influencing the overall reaction efficiency. Our data show that, compared with TPO, WO/TPO_v exhibits the lowest Gibbs free energy values for both OOH* formation and its protonation. This substantiates that the Ti^{3+}-O_v-P structure and WO incorporation not only favor OOH* formation but also significantly accelerate the reaction kinetics of the indirect $2e^-$ O_2 reduction process, thereby greatly enhancing H_2O_2 production efficiency. In conclusion, the synergistic effect of the Ti^{3+}-O_v-P structure and WO component optimizes both the thermodynamic and kinetic conditions for H_2O_2 formation by enhancing O_2 activation and promoting the transformation of key intermediates such as OOH*.

Drawing on the above data, we advance a streamlined charge transfer and redox model to explain the generation of H_2O_2 on the WO/TPO_v catalyst (Figure 6e). Upon light irradiation, the photoexcited h^+ of WO are localized by its valence band, thus expediting water oxidation and H^+ release. Meanwhile, the push-pull electronic effects caused by oxygen vacancies reconstitute the Ti^{3+}-O_v-P structure, which is beneficial for O_2 adsorption. The high-energy e^- with significantly prolonged lifetimes due to the S-scheme mechanism initiate an indirect oxygen activation mechanism, promoting the H_2O_2 generated. The synergistic coupling between prolonged photoelectron lifetime and exceptional oxygen activation capability empowers the rationally architected WO/TPO_v catalyst to deliver an outstanding H_2O_2 production performance.

4. Conclusion

In conclusion, we propose an indirect $2e^-$ oxygen activation strategy for efficient H_2O_2 photosynthesis without a sacrificial agent. By constructing a WO/TPOv catalyst rich in oxygen vacancies through structural and interfacial strategies, the optimized WO/TPOv catalyst achieves an H_2O_2 generation performance of 0.15 mmol/g/h, and achieved an SCC efficiency of 0.75%. Both experiments and theoretical calculations confirm that the excellent H_2O_2 production activity of the catalyst originates from the synergistic effect of the reconstituted Ti^{3+}-O_v-P structure activation of O_2 and the prolonged electron lifetime due to the S-scheme heterojunction. This study provides a new idea for efficient H_2O_2 photosynthesis by achieving synergistic regulation of the electron lifetime and oxygen activation ability of a single-component catalyst through dual structural and interfacial regulation strategies.

CRediT authorship contribution statement

Shanyue He: Investigation, Validation, Visualization, Formal analysis, Writing-original draft. Mei Chen and Xin Zhang: Formal analysis. Hongquan Jiang， Yang Qu and Jizhou Jiang: Funding acquisition; Supervision; Writing-review and editing. Yanduo Liu: Conceptualization; Funding acquisition; Supervision; Writing-review and editing.

Declaration of Competing Interest

The authors declare that they have no known competing financial interests or personal relationships that could have appeared to influence the work reported in this article. Jizhou Jiang is the Editor-in-Chief, and Yang Qu is an Editorial Board Member of this journal and they were not involved in the editorial review or the decision to publish this article.

Acknowledgements

The authors acknowledge support from National Natural Science Foundation of China (Nos. U24A2071, 62004143,), the Key Project of Scientific Research

Plan of Hubei Provincial Department of Education (No. D20241501).

Supplementary data

Supplementary data to this article can be found at https://doi.org/10.63823/20250203

References

[1] Yang Tao, Kong Fantao, Chen Yue, Kong Aiguo, Cui Xiangzhi, Shi Jianlin. Paired photoproduction of H_2O_2 and 3, 4-dihydroisoquinoline over covalent pyrene-(thio) urea frameworks with electron push-pull effect. Angewandte Chemie International Edition, 2025, 137, e202424110. https://doi.org/10.1002/anie.202424110

[2] Wang Qi, Ren Liping, Zhang Jie, Chen Xin, Chen Chunying, Zhang Fei, Wang Shuai, Chen Jie, Wei Jinjia. Recent progress on the catalysts and device designs for (photo)electrochemical on-site H_2O_2 production. Advanced Energy Materials, 2023, 13, 2301543. https://doi.org/10.1002/aenm.202301543

[3] Xu Yaning, Ai Shiyan, Wu Tiantian, Zhou Chengxu, Huang Qing, Li Baiyan, Tian Dan, Bu Xianhe. Bioinspired photo-thermal catalytic system using covalent organic framework-based aerogel for synchronous seawater desalination and H_2O_2production. Angewandte Chemie International Edition, 2025, 137, e202421990. https://doi.org/10.1002/anie.202421990

[4] Wang Zhenguang, Liu Shuling, Liu Yanyan, Wei Xinao, Liang Ning, Sang Zenong, Jiang Jianchun, Li Baojun. Challenges and prospects of catalyst design and environmental applications for on-site hydrogen peroxide production via diverse (photo)electrochemical reaction pathways. Small, 2025, 21, 2410612. https://doi.org/10.1002/smll.202410612

[5] Holad Yaovi, Ghosh Srabanti, W Teko, Napporn. Best practices for hydrogen peroxide (photo) electrosynthesis. Nature Sustainability, 2024, 7, 1085-1087. https://doi.org/10.1038/s41893-024-01394-8

[6] Dimitrios K. Perivoliotis, Stangel Christina, Sato Yuta, Suenaga Kazu, Tagmatarchis Nikos. Photo/Electrocatalytic hydrogen peroxide production by manganese and iron porphyrin/molybdenum disulfide nano ensembles. Small, 2022, 18, 2203032. https://doi.org/10.1002/smll.202203032

[7] Li Yang, Jia Ran, Lin Huiming, Sun Xilin, Qu Fengyu. Synthesis of $MoSe_2/CoSe_2$ nanosheets for NIR-enhanced chemodynamic therapy via synergistic *in-situ* H_2O_2 production and activation. Advanced Functional Materials, 2020, 31, 2008420. https://doi.org/10.1002/adfm.202008420

[8] Luo Xiaobo, Zhou Shiyuan, Zhou Sheng, Zhou Xinyu, Huang Jia, Liu Yingjie, Wang Danfeng, Liu Guangfeng, Gu Peiyang. Functionalized modification of conjugated porous polymers for full reaction photosynthesis of H_2O_2. Advanced Functional Materials, 2025, 35, 2415244. https://doi.org/10.1002/adfm.202415244

[9] Ou Yining, Wu Jiewei, R James, Meyer, Foston Marcus, D John, Fortner, Li Wenlu, of Photoenhanced oxidation. nC_{60} in water: exploring H_2O_2 and hydroxyl radical based reactions. Chemical Engineering Journal, 2019, 360, 665-672. https://doi.org/10.1016/j.cej.2018.12.035

[10] Qu Songying, Wu Hao, Ng Yun Hau. Clean production of hydrogen peroxide: a heterogeneous solar-driven redox process. Advanced Energy Materials, 2023, 13, 2370149. https://doi.org/10.1002/aenm.202301047

[11] Xie Jingxin, Zhong Lijie, Yang Xin, He Dequan, Lin Kanglong, Chen Xiaoxia, Wang Huan, Gan Shiyu, Niu Li. Phosphorous and selenium tuning Co-based non-precious catalysts for electrosynthesis of H_2O_2 in acidic media. Chinese Chemical Letters, 2024, 35, 108472. https://doi.org/10.1016/j.cclet.2023.108472

[12] Jiang Jizhou, Zhang Yanghanbin, Suna Wei, Peng Jiahe, Shi Weilong, Quc Yang, Liu Enzhou, Arramele, Jin Zhiliang. A review of updated red phosphorus-based photocatalysts. Composite Functional Materials, 2025, 1, 20250101. https://doi.org/10.63823/20250101

[13] Huang Donghai, Wu Tengfei, Xie Daoyue, Che Huinan, Ao Yanhui. Strategies on enhancing piezocatalysis performance of ZnO-based catalysts for aquatic pollutants degradation: A review. Composite Functional Materials, 2025, 1, 20250104. https://doi.org/10.63823/20250104

[14] Xiang Haiyan, E Jan, Lopez, Hu Travis, Cheng Jiayuan, Jiang Jizhou, Li Huimin, Liu Tang, Liu Song. Recent advances and applications of on-chip micro-/nanodevices for energy conversion and storage. Composite Functional Materials, 2025, 1, 20250102. https://doi.org/10.63823/20250102

[15] Hu Zhenyu, Yang Zhenchun, Zeng Shiqi, Wang Kun, Li Lina, Hu Chun, Zhao Yubao. Cationic surface polarization centers on ionic carbon nitride for efficient solar-driven H_2O_2 production and pollutant abatement. Chinese Chemical Letters, 2024, 35, 109526. https://doi.org/10.1016/j.cclet.2024.109526

[16] Huang Aoxue, S Roxanna, Delima, Kim Yongwook, W. Lees Eric, G. L. Fraser, Parlane, J David, Dvorak, B Michael, Rooney, P Ryan, Jansonius, G. Fink Arthur, Zhang Zishuai, P Curtis, Berlinguette. Direct H_2O_2 synthesis, without H_2 gas. Journal of the American Chemical Society, 2022, 144, 32, 14548-14554. https://doi.org/10.1021/jacs.2c03158

[17] Ogo Seiji, Yatabe Takeshi, Tome Tamon, Takenaka Riko, Shiota Yoshihito, Kato Kenji, one-pot Safe. homogeneous direct synthesis of H_2O_2. Journal of the American Chemical Society, 2023, 145, 8, 4384-4388. https://doi.org/10.1021/jacs.2c13149

[18] Xu Xiang, Zhao Yuying, Yuan Qixin, Wu Yuhan, He Jiawei, Fan Mengmeng. Porous heterostructure of h-BN/carbon as an efficient electrocatalyst for hydrogen peroxide generation. Carbon Letters, 2024, 34, 1629-1637. https://doi.org/10.1007/

s42823-024-00718-0

[19] Prasad K. Sudhakara, Naveen M. H., Manisha H., Suriani A. B., Babu T. G. Satheesh. Yoon-Bo Shim. Dual heteroatoms doped nanocarbons: electrocatalysts for hydrogen peroxide synthesis. Carbon Letters, 2024, 34, 1165-1171. https://doi.org/10.1007/s42823-023-00679-w

[20] Chen Wei, Lin Shu-Zhen, Song Zhenjun, Huang Guobo, Zhang Min. Construction of S-scheme UiO-66-NH_2/$Zn_{0.4}Cd_{0.6}S$ hybrid architectures with strong interfacial interactions triggering efficient photocatalytic H_2O_2 production, nitrogen fixation, and water splitting. Journal of Materials Science & Technology, 2025, 232, 246-256. https://doi.org/10.1016/j.jmst.2024.12.092

[21] Zhao Yanyan, Zhang Yong, Wang Libo, Ai Chenbin, Zhang Jianjun. Efficient H_2O_2 production coupling Rhodamine B degradation over covalent organic framework/g-C_3N_4 with S-scheme charge separation mechanism and fully hole-electron utilization ability. Journal of Materials Science & Technology, 2025, 229, 213-222. https://doi.org/10.1016/j.jmst.2024.12.040

[22] Sun Fanglong, Luo Yadan, Kuang Shaoping, Zhou Min, Ho Wing-Kei, Tang Hua. Ultraviolet-visible-near-infrared light responsive inorganic/organic S-scheme heterojunctions for efficient H_2O_2 production. Journal of Materials Science & Technology, 2025, 229, 287-295. https://doi.org/10.1016/j.jmst.2024.12.060

[23] Liu Yanduo, Sun Ning, Chen Shuangying, Yan Rui, Li Peng, Qu Yang, Qu Yichun, Jing Liqiang. Synthesis of nano SnO_2-coupled mesoporous molecular sieve titanium phosphate as a recyclable photocatalyst for efficient decomposition of 2, 4-dichlorophenol. Nano Research, 2018, 11, 1612-1624. https://doi.org/10.1007/s12274-017-1776-z

[24] Liu Yanduo, Zhang Xinjia, Bian Ji, Sun Jiawen, Li Zhijun, Khan Imran, Qu Yang, Li Zhibin, Jiang Zishi, Jing Liqiang. Promoted oxygen activation of layered micro-mesoporous structured titanium phosphate nanoplates by coupling nano-sized δ-MnO_2 with surface pits for efficient photocatalytic oxidation of CO. Applied Catalysis B: Environment and Energy, 2019, 254, 260-269. https://doi.org/10.1016/j.apcatb.2019.05.004

[25] Zhang Xinjia, Liu Yanduo, Chen Liqiang, Li Zhijun, Qu Yang, Wu Wei, Jing Liqiang. Porous two-dimension MnO_2-C_3N_4/titanium phosphate nanocomposites as efficient photocatalsyts for CO oxidation and mechanisms. Applied Catalysis B: Environment and Energy, 2021, 282, 119563. https://doi.org/10.1016/j.apcatb.2020.119563

[26] Zhang Xinjia, Liu Yanduo, Chen Liqiang, Li Zhijun, Wu Wei, Bian Ji, Jing Liqiang. Interface modulation of FePc/Porous $Ti(HPO_4)_2$ Z-Scheme heterojunctions with ultrafine Ag for efficiently photocatalytic CO oxidation. Small Structures, 2022, 3, 2200011. https://doi.org/10.1002/sstr.202200011

[27] Liu Yanduo, Li Xiyu, Karadas Ferdi, Gao Chao, Xiong Yujie. Synergizing multiple active sites for boosting activity and inhibiting overoxidation in photocatalytic methane valorization. ACS Materials Letters, 2025, 7, 1144-1151. https://doi.org/10.1021/acsmaterialslett.5c00088

[28] Lan Wei, Wei Banglu, Jin Yongming, Xu Shenglei, Zhou Huixin, Wu Yiran, Liu Qiu, Chen Peng, Wang Junkai, Zhao Xiaoyu, Meng Hong, Liu Lang, Wang Duozhi, Huang Haibao, Wei Yen, Zhu Quan, Yu Yuming. Efficient photocatalytic synthesis of hydrogen peroxide facilitated by triptycene-based 3D covalent organic frameworks. Small, 2025, 21, 2501327. https://doi.org/10.1002/smll.202501327

[29] Sheng Bo, Xie Yangen, Zhao Qi, Sheng Hua, Zhao Jincai. Proton reservoirs in polymer photocatalysts for superior H_2O_2 photosynthesis. Energy & Environmental Science, 2023, 16, 4612-4619. https://doi.org/10.1039/d3ee02200e

[30] Ma Jin, Peng Xiaoxiao, Zhou Zhixin, Shen Yanfei, Zhang Yuanjian. Molecular engineering of carbon nitrides for overall photosynthesis of H_2O_2. Chinese Chemical Letters, 2023, 34, 108784. https://doi.org/10.1016/j.cclet.2023.108784

[31] Zhu Qiong, Su Jingjing, Lin Guoan, Li Guisheng, Zhuo Zhiwen, Wang Weiyi, Li Jialin, Xu Xiaoxiang. Surface indium vacancies promote photocatalytic H_2O_2 production over In_2S_3. Nature Communications, 2025, 16, 10501. https://doi.org/10.1038/s41467-025-65538-w

[32] Jiang Hongquan, Liu Yanduo, Zang Shuying, Li Jingshen, Wang Haiyan. Microwave-assisted hydrothermal synthesis of Nd, N, and P tri-doped TiO_2 from $TiCl_4$ hydrolysis and synergetic mechanism for enhanced photoactivity under simulated sunlight irradiation. Materials Science in Semiconductor Processing, 2015, 40, 822-831. https://doi.org/10.1016/j.mssp.2015.07.069

[33] Jiang Hongquan, Liu Yanduo, Li Jingshen, Wang Haiyan. Synergetic effects of lanthanum, nitrogen and phosphorus tri-doping on visible-light photoactivity of TiO_2 fabricated by microwave-hydrothermal process. Journal of Rare Earths, 2016, 34, 604-613. https://doi.org/10.1016/S1002-0721(16)60068-6

[34] Morra Elena, Giamello Elio, Antinucci Giuseppe, D'Amore Maddalena, Busico Vincenzo, Chiesa Mario. Sabine Van Doorslaer, Probing the coordinative unsaturation and local environment of Ti^{3+} sites in an activated High-Yield Ziegler-Natta catalyst. Angewandte Chemie International Edition, 2015, 54, 4857-4860. https://doi.org/10.1002/anie.201412052

[35] Feng Ningdong, Lin Huiwen, Song Hui, Yang Longxiao, Tang Daiming, Deng Feng, Ye Jinhua. Efficient and selective photocatalytic CH_4 conversion to CH_3OH with O_2 by controlling overoxidation on TiO_2. Nature Communications, 2021, 21, 4652. https://doi.org/10.1038/s41467-021-24912-0

[36] Liu Yanduo, Li Mengwei, Guo Jianing, Jin Ge, Yin Yue, Cui Yu, Sun Tong. Na-Ru bimetallic functional sites promote photo-driven CO_2 directed conversion into CH_4. Journal of Colloid and Interface Science, 2024, 667, 22-31, https://doi.org/10.1016/j.jcis.2024.04.068

[37] Liu Yanduo, Li Jiadong, Dong Xianglan, Dai Lina, Zhang

Enqi. Au depositing and Mg doping synergistically regulates an In_2O_3 photocatalyst for promoting CO_2 reduction and CH_4 exclusive generation. Inorganic Chemistry Frontiers, 2024, 11, 5310-5318. https://doi.org/10.1039/d4qi01381f

[38] Huang Yue, Zhang Jinfeng, Ruzimuradov Olim, Mamatkulov Shavkat, Dai Kai, Low Jingxiang. Selective oxygen vacancy engineering for shrinking the potential barrier of S-scheme heterojunction toward highly efficient photocatalytic CO_2 conversion. Composite Functional Materials, 2025, 1, 20250103. https://doi.org/10.63823/20250103

[39] Guo Xin, Liu Yanduo, Yang Yang, Mu Zhiyuan, Wang Ying, Zhang Shuai, Wang Shuai, Hu Yufeng, Liu Zhichang. Effective visible-light excited charge separation in all-solid-state Ag bridged $BiVO_4/ZnIn_2S_4$ core-shell structure Z-Scheme nanocomposites for boosting photocatalytic organics degradation. Journal of Alloys and Compounds, 2021, 887, 161389. https://doi.org/10.1016/j.jallcom.2021.161389

[40] Li Shijie, Li Rui, Dong Kexin, Liu Yanping, Yu Xin, Li Wenyao, Liu Tong, Zhao Zaiwang, Zhang Mingyi, Zhang Bin, Chen Xiaobo. Self-floating $Bi_4O_5Br_2$/P-doped C_3N_4/carbon fiber cloth with S-scheme heterostructure for boosted photocatalytic removal of emerging organic contaminants. Chinese Journal of Catalysis, 2025, 76, 37-49. https://doi.org/10.1016/S1872-2067(25)64780-2

[41] Guo Xin, Sun Xiaojie, Wang Zhiyuan, Zhang Jiahui, Liu Zhichang, Hu Yufeng, Liu Yanduo. *In-situ* growth of Z-Scheme Ag/PPy/$BiVO_4$ core-shell structure for efficient CO_2 photoreduction into hydrocarbon fuels. Fuel, 2023, 343, 128004. https://doi.org/10.1016/j.fuel.2023.128004

[42] Li Xibao, Wan Yiyang, Deng Fang, Zhou Yingtang, Chen Pinghua, Dong Fan, Jiang Jizhou. Advances in Z-scheme and S-scheme heterojunctions for photocatalytic and photoelectrocatalytic H_2O_2 production. Chinese Chemical Letters, 2025, 36, 111418. https://doi.org/10.1016/j.cclet.2025.111418

[43] Dai Lina, Li Qiang, Dong Xianglan, Zhang Enqi, Hu Yufeng, Guo Xin, Liu Yanduo. Smooth charge transfer at the Ag_2MoO_4/Mn-Fe PBAs S-Scheme interface for photo-driven CO_2 reduction. Fuel, 2025, 395, 135210. https://doi.org/10.1016/j.fuel.2025.135210

[44] Ding Lu, Lei Minjun, Wang Tian, Wang Jing, Jin Zhiliang. Graphdiyne coordinated CoMo-MOF formed S-scheme heterojunction boosting photocatalytic hydrogen production. Carbon Letters, 2024, 34, 2099-2112. https://doi.org/10.1007/s42823-024-00743-z

[45] Dai Lina, Dong Xianglan, Zhang Enqi, Liu Yanduo. High-energy-level electron injection in $ZnWO_4$/ZnO photocatalysts for efficient methane-to-methanol conversion. Fuel, 2025, 396, 135297. https://doi.org/10.1016/j.fuel.2025.135297

[46] Liu Yanduo, Chen Yihong, Jiang Wenbin, Kong Tingting, H C Camargo Pedro, Gao Chao, Xiong Yujie. Highly efficient and selective photocatalytic nonoxidative coupling of methane to ethylene over Pd-Zn synergistic catalytic sites. Research, 2022, 9831340. https://doi.org/10.34133/2022/9831340

[47] Li Bin, Sun Liqun, Bian Ji, Sun Ning, Sun Jiawen, Chen Liqiang, Li Zhijun, Jing Liqiang. Controlled synthesis of novel Z-scheme iron phthalocyanine/porous WO_3 nanocomposites as efficient photocatalysts for CO_2 reduction. Applied Catalysis B: Environment and Energy, 2020, 270, 118849. https://doi.org/10.1016/j.apcatb.2020.118849

[48] Li Jiadong, Zhang Xuliang, Raziq Fazal, Wang Jinshuang, Liu Chong, Liu Yanduo, Sun Jiawen, Yan Rui, Qu Binhong, Qin Chuanli, Jing Liqiang. Improved photocatalytic activities of g-C_3N_4 nanosheets by effectively trapping h^+ with halogen-induced surface polarization and 2, 4-dichlorophenol decomposition mechanism. Applied Catalysis B: Environment and Energy, 2017, 218, 60-67. https://doi.org/10.1016/j.apcatb.2017.06.038

[49] Jin Cheng, Shen Hao, Li Jinhe, Guo Xinge, Rao Shaosheng, Yang Wenqiang, Liu Qinqin, Sun Zhongti, Yang Juan. Isolated Ni atoms for enhanced photocatalytic H_2O_2 performance with 1. 05% solar-to-chemical conversion efficiency in pure water. Nano Letters, 2024, 24, 14484-14492. https://doi.org/10.1021/acs.nanolett.4c04573

[50] Hou Huilin, Zeng Xiangkang, Zhang Xiwang. Production of hydrogen peroxide by photocatalytic processes. Angewandte Chemie International Edition, 2019, 59, 17356-17376. https://doi.org/10.1002/anie.201911609

[51] Zhao Yanyan, Zhang Shumin, Wu Zhen, Zhu Bicheng, Sun Guotai, Zhang Jianjun. Regulation of d-band center of TiO_2 through fluoride doping for enhancing photocatalytic H_2O_2 production activity. Chinese Journal of Catalysis, 2024, 60, 219-230. https://doi.org/10.1016/S1872-2067(23)64645-5

[52] Zhang Yuanzheng, Liang Chao, Feng Haopeng, Liu Wei. Nickel single atoms anchored on ultrathin carbon nitride for selective hydrogen peroxide generation with enhanced photocatalytic activity. Chemical Engineering Journal, 2022, 446, 137379. https://doi.org/10.1016/j.cej.2022.137379

[53] Zhang Yunchao, Pan Jinkang, Ni Xiang, Mo Feiqi, Xu Yuanguo, Dong Pengyu. Revealing the dynamics of charge carriers in organic/inorganic hybrid FS-COF/WO_3 S-scheme heterojunction for boosted photocatalytic hydrogen evolution. Chinese Journal of Catalysis, 2025, 74, 250-263. https://doi.org/10.1016/S1872-2067(25)64664-X

[54] Li Shijie, Li Xinyu, Liu Yanping, Zhang Peng, Zhang Junlei, Zhang Bin. Interfacial engineering of a plasmonic $Ag/Ag_2CO_3/C_3N_5$ S-scheme heterojunction for high-performance photocatalytic degradation of antibiotics. Chinese Journal of Catalysis, 2025, 72, 130-142. https://doi.org/10.1016/S1872-2067(25)64652-3

[55] Yi Futao, Liu Ying, Chen Yao, Zhu Jiahao, He Quanguo, Yang Chun, Ma Dongge, Liu Jun. Dual S-Scheme g-C_3N_4/Ag_3PO_4/g-C_3N_5 photocatalysts for removal of tetracycline pollutants through enhanced molecular oxygen activation. Chinese Chemical Letters, 2025, 36, 110544. https://doi.org/10.1016/j.cclet.2024.110544

[56] Dai Lina, Wang He, Cui Liru, Liu Yanduo. Built-in electric field driven rapid charge transfer at the Ag_3PO_4/Cu-Co PBAs S-Scheme interface for CO_2 reduction into chemical energy. Renewable Energy, 2025, 247, 123093. https://doi.org/10.1016/j.renene.2025.123093

[57] Zhang Liuyang, Zhang Jianjun, Yu Huogen, Yu Jiaguo. Emerging S-Scheme photocatalyst. Advanced Materials, 2022, 34, 2107668. https://doi.org/10.1002/adma.202107668

[58] Liu Xiaodong, Li Yuanfei, Wang Huanli, Liu Jiayuan, Fu Jingchuan, Liu Jia, Li Shijie. *In situ* construction of N-rich carbon nitride (C_3N_5)/silver phosphate (Ag_3PO_4) S-scheme heterojunctions for the efficient photocatalytic removal of levofloxacin antibiotic and RhB. Carbon Letters, 2024, 34, 1995-2011. https://doi.org/10.1007/s42823-024-00741-1

[59] Ruan Xiaowen, Huang Chengxiang, Cheng Hui, Zhang Zhiquan, Cui Yi, Li Zhiyun, Xie Tengfeng, Ba Kaikai, Zhang Haiyan, Zhang Lei, Zhao Xiao, Leng Jing, Jin Shengye, Zhang Wei, Zheng Weitao. Sai Kishore Ravi, Zhifeng Jiang, Xiaoqiang Cui, Jiaguo Yu. A twin S-Scheme artificial photosynthetic system with self-assembled heterojunctions yields superior photocatalytic hydrogen evolution rate. Advanced Materials, 2023, 35, 2209141. https://doi.org/10.1002/adma.202209141

[60] Cheng Chang, Zhang Jianjun, Zhu Bicheng, Liang Guijie, Zhang Liuyang, Yu Jiaguo. Verifying the charge-transfer mechanism in S-Scheme heterojunctions using femtosecond transient absorption spectroscopy. Angewandte Chemie International Edition, 2023, 62, e202218688. https://doi.org/10.1002/anie.202218688

[61] Yang Yi, Zhou Xin, Gu Miaoli, Cheng Bei, Wu Zhen, Zhang Jianjun. Investigating the charge transfer mechanism of ZnSe QD/COF S-Scheme photocatalyst for H_2O_2 production by using femtosecond transient absorption spectroscopy. Chinese Journal of Catalysis, 2024, 63, 258-269. https://doi.org/10.1016/s1872-2067(24)60069-0

[62] Li Zhi, Li Ru, Liu Rui, Zhang Wenjie, Wan Yong, Sun Yuze, Yang Lei, Long Yunze. A beaded g-C_3N_4/$CoFe_2O_4$ nanofibers for efficient adsorbing and catalytical degrading multiple pollutants. Carbon Letters, 2025, 35, 1187-1203. https://doi.org/10.1007/s42823-025-00863-0

[63] Liu Maosong, Lei Zhihao, Lv Xianhe, Song Xiaoxue, Zhang Long, Li Shun, Sun Tao, Li Li, Hui Jianing, Zhang Wenyong, Yee Wong Siew, Li Xu, Xia Guangjie, Zhang Jianming, Sun Shuhui. Enhancing the ORR durability of single atomic Fe-N_4 active sites with implanted SiO_2 nanoparticles as radical and H_2O_2 inhibitors. Nature Communications, 2025, 16, 10178. https://doi.org/10.1038/s41467-025-65194-0

[64] Xu Feiyan, Zhao Feifan, Deng Xianyu, Zhang Jinfeng, Zhang Jianjun, Ai Chenbin, Yu Jiaguo, García Hermenegildo. Integrating S-scheme photocatalysis with tandem carbonylation: A green and scalable strategy for CO_2 valorization. Nature Communications, 2025, 16, 6882. https://doi.org/10.1038/s41467-025-60961-5

[65] Gao Tengyuan, Shi Dan, Liu Xiufan, Wu Xinhe, Wang Guohong. Investigating the charge transfer mechanism of 1D/2D ZnO/$SnIn_4S_8$ S-scheme heterojunction for efficient photocatalytic hydrogen evolution. Journal of Materials Science & Technology, 2026, 251, 241-251. https://doi.org/10.1016/j.jmst.2025.07.006

[66] Han Qing, Wu Chongbei, Jiao Haimiao, Xu Ruoyu, Wang Yuze, Xie Jijia, Guo Qian, Tang Junwang. Rational design of high-concentration Ti^{3+} in porous carbon-doped TiO_2 nanosheets for efficient photocatalytic ammonia synthesis. Advanced Materials, 2021, 33, 2008180. https://doi.org/10.1002/adma.202008180

[67] M. Comer Benjamin, J. Medford Andrew. Analysis of photocatalytic nitrogen fixation on rutile TiO_2(110). ACS Sustainable Chemistry & Engineering, 2018, 6, 4648-4660, https://doi.org/10.1021/acssuschemeng.7b03652

[68] Chinthala Praveen Kumar. Neeruganti Obularajugari Gopal, Ting Chung Wang, Mingshow Wong, Shyue Chu Ke. EPR investigation of TiO_2 nanoparticles with temperature-dependent properties. The Journal of Physical Chemistry B, 2006, 110, 5223-5229. https://doi.org/10.1021/jp057053t

[69] Mohajernia Shiva, Andryskova Pavlina, Zoppellaro Giorgio, Hejazi Seyedsina, Kment Stepan, Zboril Radek, Schmidt Jochen, Schmuki Patrik. Influence of Ti^{3+} defect-type on heterogeneous photocatalytic H_2 evolution activity of TiO_2. Journal of Materials Chemistry A, 2020, 8, 1432-1442. https://doi.org/10.1039/C9TA10855F

[70] Yin Yue, Dong Xianglan, Dai Lina, Zhang Enqi, Liu Yanduo. Hydroxyl and amino co-modified imidazole based ionic liquid functionalized TS-1 molecular sieve for efficient CO_2 capture. Separation and Purification Technology, 2025, 358, 130393. https://doi.org/10.1016/j.seppur.2024.130393

[71] Liu Qinghua, Guo Xin, Hu Yufeng, Li Qiang, Jiao Jianhao, Meng Zitao, An Yongqi, Tang Xuqi, Yuan Maojie, Wang Bingcan, Qin Yucai, Liu Yanduo. Functional ionic liquid anchored TS-1 molecular sieve with multiple adsorption sites for efficient capture and separation of CO_2 in flue gas systems. Separation and Purification Technology, 2025, 360, 130920. https://doi.org/10.1016/j.seppur.2024.130920

[72] Deng Danni, Wang Jinxian, Wang Meng, Wang Yuchao, Jiang Jiabi, Chen Yingbi, Bai Yu, Wu Qiumei, Lei Yongpeng. Accelerated O_2 adsorption and stabilized *OOH for electrocatalytic H_2O_2 production. Journal of Materials Science & Technology, 2025, 227, 76-81. https://doi.org/10.1016/j.jmst.2024.12.017

[73] Dai Lina, Wang He, Liu Yanduo, Cui Liru. Ag-Mg tandem sites co-modified ultrathin ZnO achieving adsorption and activation synergistic effects for light-driven methane selective conversion. Chemical Engineering Journal, 2025, 512, 162380. https://doi.org/10.1016/j.cej.2025.162380

[74] Dong Xianglan, Wang He, Liu Yanduo, Cui Liru. Mg-Pd coexisted adsorption and activation tandem sites for methane photocoupling into ethane by oxygen medium. Chemical

Engineering Journal, 2025, 515, 163829. https://doi.org/10.1016/j.cej.2025.163829

[75] Rouillé G., Millot G., Saint-Loup R., Berger H.. High-resolution stimulated Raman spectroscopy of O_2. Journal of Molecular Spectroscopy, 1992, 154, 372-382. https://doi.org/10.1016/0022-2852(92)90215-A

[76] Xiao Jun, Yu Shenjie, Wang Haijian, Pan Duo, Li Tianmi, Yang Juan, Wen Zhenhai, Ci Suqin. Enhanced efficiency in organic wastewater treatment by synergetic cathodic produced $H_2O_2$and anodic oxidation. Renewable Energy, 2026, 256, 124321. https://doi.org/10.1016/j.renene.2025.124321

[77] H Phebe, G.H. Dennis, Hetterscheid. Selective electrochemical H_2O_2 production by a molecular copper catalyst: A crucial relation between reaction rate and mass transport. Chem Catalysis, 2024, 4, 101069. https://doi.org/10.1016/j.checat.2024.101069

[78] Zhao Erzhuo, Xue Wendan, Qin Shuhan, Guo Yang, Xin Xin, Wang Huijiao, Zhang Yinqiao, Zuo Sijin. A review of H_2O_2 electrosynthesis by 2-electron ORR and 2-electron WOR: From catalysts to electrochemical cells. Coordination Chemistry Reviews, 2025, 545, 217042. https://doi.org/10.1016/j.ccr.2025.217042

[79] Foo Joel Jie, Ng Sue Faye, Kok Steven Hao, Zeng Xianhai, Tan Lling Lling, Ong Wee Jun. Synergistic potassium intercalation and cyano group modification on crystalline carbon nitride homojunction towards dual-functional photoredox coupling of H_2O_2 and benzaldehyde production. Chemical Engineering Journal, 2025, 505, 158992. https://doi.org/10.1016/j.cej.2024.158992

[80] Gotti Guillaume, Evrard David, Gros Pierre. Simultaneous electrochemical detection of oxygen (O_2) and hydrogen peroxide (H_2O_2) in neutral media. International Journal of Electrochemical Science, 2023, 18, 100262. https://doi.org/10.1016/j.ijoes.2023.100262

[81] Wang Xinyao, Yang Xiaowei, Zhao Chen, Pi Yutong, Li Xiaobo, Jia Zhongfan, Zhou Si, Zhao Jijun, Wu Limin, Liu Jian. Ambient preparation of benzoxazine-based phenolic resins enables long-term sustainable photosynthesis of hydrogen peroxide. Angewandte Chemie International Edition, 2023, 62, e202302829. https://doi.org/10.1002/anie.202302829

[82] Liu Ping, Liang Teng, Li Yutong, Zhang Ziqing, Li Zhuo, Bian Ji, Jing Liqiang. Photocatalytic H_2O_2 production over boron-doped g-C_3N_4 containing coordinatively unsaturated FeOOH sites and CoO_x clusters. Nature Communications, 2024, 15, 9224. https://doi.org/10.1038/s41467-024-53482-0

[83] Xu Shuaifei, Dai Huichao, Zhu Shaolong, Wu Yanchao, Sun Mingxuan, Chen Yuan, Fan Kun, Zhang Chenyang, Wang Chengliang, Hu Wenping. A branched dihydrophenazine-based polymer as a cathode material to achieve dual-ion batteries with high energy and power density. eScience, 2021, 1, 60-68. https://doi.org/10.1016/j.esci.2021.08.002

[84] Chen Liang, Wang Lei, Wan Yangyang, Zhang Ying, Qi Zeming, Wu Xiaojun, Xu Hangxun. Acetylene and diacetylene functionalized covalent triazine frameworks as metal-free photocatalysts for hydrogen peroxide production: a new two-electron water oxidation pathway. Advanced Materials, 2020, 32, 1904433. https://doi.org/10.1002/adma.201904433

[85] Liu Youxing, Li Lu, Sang Zhiyuan, Tan Hao, Ye Na, Sun Chenglong, Sun Zongqiang, Luo Mingchuan, Guo Shaojun. Enhanced hydrogen peroxide photosynthesis in covalent organic frameworks through induced asymmetric electron distribution. Nature Synthesis, 2025, 4, 134-141. https://doi.org/10.1038/s44160-024-00644-z

[86] Zhang Kailian, Dan Meng, Yang Jingfei, Wu Fengxiu, Wang Leigang, Tang Hua, Liu Zhaoling. Surface energy mediated sulfur vacancy of $ZnIn_2S_4$ atomic layers for photocatalytic H_2O_2 production. Advanced Functional Materials, 2023, 33, 2302964. https://doi.org/10.1002/adfm.202302964

[87] Fu Fan, Liu Yongxin, Liu Mingliang, Li Zhengguang, Zhong Wanying, Li Yaqin, Li Kaixiu, Wang Jun, Huang Yongchao, Li Yiming, Liu Wei, Zhang Yi, Xiang Kaisong, Liu Hui, Wang Pingshan, Liu Die. Non-noble metal single-molecule photocatalysts for the overall photosynthesis of hydrogen peroxide. Journal of the American Chemical Society, 2025, 147, 6390-6403. https://doi.org/10.1021/jacs.4c09445

[88] Zhang Yaning, Pan Chengsi, Bian Gaoming, Xu Jing, Dong Yuming, Zhang Ying, Lou Yang, Liu Weixu, Zhu Yongfa. H_2O_2 generation from O_2 and H_2O on a near-infrared absorbing porphyrin supramolecular photocatalyst. Nature Energy, 2023, 8, 361-371. https://doi.org/10.1038/s41560-023-01218-7

[89] J. Lewis Richard, Ueura Kenji, Liu Xi, Fukuta Yukimasa, E. Davies Thomas, J. Morgan David, Chen Liwei, Qi Jizhen, Singleton James, K Jennifer., Edwards, J. Freakley Simon, J. Kiely Christopher, Yamamoto Yasushi. Graham J. Hutchings. Highly efficient catalytic production of oximes from ketones using *in situ*-generated H_2O_2. Science, 2022, 376, 615-620. https://doi.org/10.1126/science.abl4822

[90] Liu Binyao, Du Jinyan, Ke Gaili, Jia Bi, Huang Yujie, He Huichao, Zhou Yong, Zou Zhigang, Boosting. O_2 reduction and H_2O dehydrogenation kinetics: surface N-Hydroxymethylation of g-C_3N_4 photocatalysts for the efficient production of H_2O_2. Advanced Functional Materials, 2022, 32, 2111125. https://doi.org/10.1002/adfm.202111125

[91] Zhi Qianjun, Liu Wenping, Jiang Rong, Zhan Xiaoning, Jin Yucheng, Chen Xin, Yang Xiya, Wang Kang, Cao Wei, Qi Dongdong, Jiang Jianzhuang. Piperazine-linked metalphthalocyanine frameworks for highly efficient visible-light-driven H_2O_2 photosynthesis. Journal of the American Chemical Society, 2022, 144, 21328-21336. https://doi.org/10.1021/jacs.2c09482